The Role of Surface Drag in Tornadogenesis within an Idealized Supercell Simulation

BRETT ROBERTS AND MING XUE

Center for Analysis and Prediction of Storms, and School of Meteorology, University of Oklahoma, Norman, Oklahoma

ALEXANDER D. SCHENKMAN

Center for Analysis and Prediction of Storms, University of Oklahoma, Norman, Oklahoma

DANIEL T. DAWSON II

Purdue University, West Lafayette, Indiana

(Manuscript received 2 November 2015, in final form 2 May 2016)

ABSTRACT

To investigate the effect of surface drag on tornadogenesis, a pair of idealized simulations is conducted with 50-m horizontal grid spacing. In the first experiment (full-wind drag case), surface drag is applied to the full wind; in the second experiment (environmental drag case), drag is applied only to the background environmental wind, with storm-induced perturbations unaffected. The simulations are initialized using a thermal bubble within a horizontally homogeneous background environment that has reached a balance between the pressure gradient, Coriolis, and frictional forces. The environmental sounding is derived from a prior simulation of the 3 May 1999 Oklahoma tornado outbreak but modified to account for near-ground frictional effects. In the full-wind drag experiment, a tornado develops around 25 min into the simulation and persists for more than 10 min; in the environmental-only drag experiment, no tornado occurs. Three distinct mechanisms are identified by which surface drag influences tornadogenesis. The first mechanism is the creation by drag of near-ground vertical wind shear (and associated horizontal vorticity) in the background environment. The second mechanism is generation of near-ground crosswise horizontal vorticity by drag on the storm scale as air accelerates into the low-level mesocyclone; this vorticity is subsequently exchanged into the streamwise direction and eventually tilted into the vertical. The third mechanism is frictional enhancement of horizontal convergence, which strengthens the low-level updraft and stretching of vertical vorticity. The second and third mechanisms are found to work together to produce a tornado, while baroclinic vorticity plays a negligible role.

1. Introduction

Despite several decades of intense focus from the research community, our understanding of the physical mechanisms responsible for supercell tornadogenesis remains incomplete. Horizontal vorticity in the prestorm environment has been well established as the primary source for midlevel rotation in supercells (Davies-Jones 1984); by contrast, various potential sources for near-ground vorticity in a tornadic supercell continue to be investigated. A fundamental question underlying much of the contemporary research on this topic is the following: Does the vertical vorticity associated with tornadoes originate primarily from a baroclinic source or some other source? The earliest numerical modeling studies of supercells which resolved near-ground circulations (Klemp and Rotunno 1983; Rotunno and Klemp 1985) emphasized the importance of storm-generated baroclinic vorticity associated with a cool, rainy downdraft. Subsequent observational studies, however, revealed that cooler downdrafts are associated with a decreased likelihood for tornadogenesis; this is true for both the forward-flank (Shabbott and

Corresponding author address: Ming Xue, Center for Analysis and Prediction of Storms, University of Oklahoma, 120 David L. Boren Blvd., Norman, OK 73072.
E-mail: mxue@ou.edu

DOI: 10.1175/JAS-D-15-0332.1

© 2016 American Meteorological Society

Markowski 2006) and rear-flank (Markowski et al. 2002; Grzych et al. 2007) downdraft regions. To reconcile these findings with the baroclinic mechanism, Markowski et al. (2008) hypothesized the existence of a ''goldilocks phenomenon'' wherein the cold pool must be of sufficient strength to generate baroclinic vorticity exceeding some threshold but not so strong as to inhibit upward vertical acceleration of parcels (and hence vertical stretching within an incipient vortex) due to reduced buoyancy. Thermodynamic observations made by Markowski et al. (2012) of the 5 June 2009 Goshen County, Wyoming, tornadic supercell supported this theory; sensitivity tests of idealized simulations in Markowski and Richardson (2014) similarly found that an ''intermediate'' cold pool strength was optimal for generating a strong near-surface vortex.

The relative roles of environmental barotropic vorticity (brought into the storm from the environment) and baroclinically generated vorticity in producing strong low-level rotation in supercell storms have recently been investigated in idealized simulations by Dahl et al. (2014, hereafter D14) and Dahl (2015, hereafter D15), using 250-m horizontal grid spacing (which can at most simulate tornado-like vortices, not tornadoes themselves). Using a Lagrangian technique for tracking the evolution of vortex line segments in a simulated tornadic supercell, D14 determined that the horizontal vorticity ultimately tilted into the vertical in near-surface vortices was dominated by the baroclinic component; very near the ground, the barotropic vorticity component generally remained nearly horizontal, in line with the local velocity vector. The importance of the baroclinic mechanism was confirmed using a similar methodology in D15, even for storm environments that contained large crosswise environmental vorticity. Thus, the work of D14 and D15 supports the notion that baroclinically generated vorticity is paramount for developing strong rotation near the ground in supercells.

The aforementioned idealized tornadic supercell simulations, including D14 and D15, employed free-slip lower boundary conditions. As such, surface drag (a potentially important source of horizontal vorticity) was neglected, except for its role in producing near-surface vertical wind shear in the environment. Within the context of idealized tornado vortex simulations, researchers employed no-slip lower boundary conditions (and hence included surface drag) in studies of tornadoes as early as the 1990s (Trapp and Fiedler 1995; Lewellen et al. 1997; Trapp 2000). However, these highly idealized experiments typically used artificial, steady-state forcing mechanisms (for both the supporting updraft and the source of vertical vorticity) in lieu of dynamic forcing that would develop within realistic simulations of tornadic storms. Certain questions therefore cannot be answered based on such simulations.

Wicker and Wilhelmson (1993, hereafter WW93) performed supercell storm simulations in which two fine-mesh (120-m grid spacing) simulations were nested within a coarse-mesh (600-m grid spacing) simulation just prior to the development of a strong low-level mesocyclone; surface drag was included in one of the fine-mesh simulations. The results of WW93 demonstrated a contraction of the diameter of a tornado-like vortex (TLV) and substantially stronger low-level updraft around the vortex when surface drag was included, although computational limitations of the time prohibited a more holistic approach with drag enabled throughout the storm's life cycle. Adlerman and Droegemeier (2002) explored the effects of surface drag on mesocyclone evolution as part of a broad parameter-space numerical study, finding more steady-state, persistent mesocyclones with increasing drag coefficient; however, their simulations were limited to a relatively coarse mesocyclone-resolving resolution ($x = 500\,\mathrm{m}$), and the authors were forced to use a relatively small drag coefficient ($C_d = 10^{-3}$) to obtain a sustained supercell. When a drag coefficient typical of that over land ($C_d = 10^{-2}$) was used, a mesocyclone did not develop. In Adlerman and Droegemeier (2002), the drag was applied to perturbation winds, and the base state was assumed to be in balance with friction (but, unlike the present study, no adjustment procedure was applied to ensure that the base state actually was in balance with the model's parameterization of surface drag).

Not until very recent years have real-case simulations incorporating heterogeneous observation-based initial and boundary conditions been performed at tornado-resolving resolutions; such real-case simulations usually include surface drag. Mashiko et al. (2009) modeled a tornadic minisupercell associated with a typhoon at a 50-m grid spacing by starting from mesoscale numerical weather prediction (NWP) model initial conditions; the authors performed quantitative vorticity budget analyses along parcel trajectories and suggested that preexisting horizontal vorticity in the environment was the dominant source of tornadic vorticity. The direct generation of horizontal vorticity by friction was found to be negligible in their case. A point worth noting is that, in their tropical cyclone environment, the low-level vertical wind shear of about $20\,\mathrm{m\,s^{-1}}$ in the lowest 500 m above ground level (AGL) was much larger than that typical of continental tornadic supercell environments. Additionally, the strong near-surface vertical wind shear in the environment can be attributed to surface drag as the strong typhoon circulation moved over land. In other words, large vertical wind shear (and horizontal vorticity) had already been generated by surface drag before the near-surface air parcels entered the tornadic minisupercell.

Schenkman et al. (2012) simulated a TLV associated with a mesovortex within a mesoscale convective system in Oklahoma, implicating surface drag in the development of a horizontal rotor. The circulation associated with the rotor dramatically enhanced low-level convergence and updraft near the mesovortex center, leading to the development of the TLV. Xue et al. (2014) reported on a successful simulation of a tornadic supercell and embedded tornadoes in central Oklahoma on 8 May 2003 at 50-m grid spacing. Their simulation started from an initial condition that assimilated real radar observations. Through detailed vorticity diagnostic analyses along parcel trajectories, Schenkman et al. (2014, hereafter S14) showed that in the same simulation, surface drag played a significant, if not dominant, role in the development of two simulated tornadoes within the supercell. Specifically, surface drag generated large horizontal vorticity, which was imported by tornado-entering parcels and then tilted into the vertical. For the first tornado, drag generated horizontal vorticity within an internal rear-flank downdraft (RFD) surge and within low-level inflow. For the second tornado, drag similarly enhanced horizontal vorticity in the low-level inflow of a new developing convective cell. In both cases, horizontal vorticity enhancement by drag was associated with a region of accelerating low-level flow. Most recently, Nowotarski et al. (2015) performed idealized simulations of a supercell that included surface drag and found that convective rolls within the boundary layer can modulate mesocyclone intensity, depending upon their orientation. Their study did not address the role of frictionally generated vorticity in low-level mesocyclone development, however.

The goal of the present study is to identify and analyze mechanisms by which surface drag may influence supercell tornadogenesis using an idealized experimental design that reduces some of the complexity of real-data cases. A pair of idealized simulations of a supercell is conducted, with the environment defined by a sounding derived from a real-data simulation of the 3 May 1999 tornado outbreak in Oklahoma. This sounding ensures that the far-field storm environment in the idealized simulation remains more or less unchanged in the presence of surface drag. The two simulations are differentiated by the formulation of surface drag employed: in one, drag is applied to the full horizontal wind components; in the other, drag is applied only to the base-state horizontal wind components (as defined by the environmental sounding). Effectively, no surface drag acts on the storm-induced perturbation flow in the second experiment, while the perturbation flow in the first experiment is subject to drag.

The remainder of this paper is organized as follows: Section 2 describes the model setup and the methods used for establishing the steady-state background sounding. Section 3 presents and discusses the results of the simulations. Section 4 includes a summary, conclusions, and suggests directions for future research.

2. Experimental setup

a. Model setup and parameters

The nonhydrostatic Advanced Regional Prediction System (ARPS) (Xue et al. 2000, 2001) is used to produce the pair of idealized simulations. The simulation domain is 64 km × 96 km in the horizontal and 16 km in the vertical, with a Rayleigh sponge layer applied above 12 km AGL. Grid spacing is 50 m in the horizontal. The vertical grid spacing increases from 20 m at the surface to 400 m above 10 km AGL, with a total of 83 levels. The lower boundary is flat, and the first level of scalar variables (as well as horizontal momentum) is at 10 m AGL. Advection is fourth order in the horizontal and vertical. Parameterization of microphysics follows the five-species formulation of Lin et al. (1983) with a modified rain intercept parameter N_{0r} of $2 \times 10^6\,\mathrm{m}^{-4}$; values reduced from the default of $8 \times 10^6\,\mathrm{m}^{-4}$ have yielded more realistic cold pools and stronger TLVs in previous supercell simulations (Snook and Xue 2008; Dawson et al. 2010, hereafter DA10, 2015). Subgrid-scale turbulence is parameterized using the 1.5-order TKE formulation of Moeng and Wyngaard (1988), and fourth-order computational mixing is employed. Both experiments are integrated forward in time for 7200 s, although the results presented herein will focus on the first 2400 s.

The two experiments, to be referred to as full-wind friction (FWFRIC) and environment-only friction (EnvFRIC), are differentiated solely by the surface drag formulation. The purpose of these experiments is to discriminate between effects from the frictionally induced near-ground wind shear in the background environment versus effects from friction acting on the storm-induced wind perturbations. In both experiments, surface drag acts on the environmental flow, but only in FWFRIC does drag act on the storm-induced perturbation winds. The environmental flow, as will be shown below, is balanced by the horizontal pressure gradient force (PGF), the Coriolis force, and the frictional force.

In the ARPS, surface drag is introduced through horizontal momentum stresses defined at the surface:

$$-\tau_{13}(z=0) = \rho C_d V_h u, \quad (1)$$

$$-\tau_{23}(z=0) = \rho C_d V_h v, \quad (2)$$

where τ_{13} and τ_{23} are components of the Reynolds stress tensor that appear in the subgrid-scale turbulence parameterization; C_d is the dimensionless drag coefficient valid at 10 m AGL; u and v are the ground-relative horizontal wind components; and V_h is the ground-relative horizontal wind speed. In FWFRIC, the standard ARPS formulation for surface drag is used, as specified in (1) and (2). In EnvFRIC, surface drag operates only on the base-state wind components as defined by the environmental sounding; thus, storm-induced deviations from the environmental profile are not subject to surface drag. Mathematically, this is represented as

$$-\tau_{13}(z=0) = \rho C_d \overline{V_h}\,\overline{u}, \quad (3)$$

$$-\tau_{23}(z=0) = \rho C_d \overline{V_h}\,\overline{v}, \quad (4)$$

where $\overline{u}$ and $\overline{v}$ are the base-state wind components (as defined by the environmental sounding), and $\overline{V_h}$ is the corresponding wind speed. In the simulations presented herein, the drag coefficient C_d is set to 0.01, which is on the high end of representative values over land. The use of a fixed value, rather than parameterized values as used in S14, simplifies the interpretation of the results of our idealized simulations.

For both experiments, the horizontally homogeneous environment is based on a sounding extracted from a real-data simulation of the 3 May 1999 central Oklahoma tornado outbreak from Dawson et al. (2010, hereafter DA10). The sounding comes from the inflow region of the simulated storm valid at 2300 UTC and was also used to initialize subsequent idealized simulations in DA10, as it was believed to better represent the storm environment than the closest available observed sounding (at Norman, Oklahoma). In this study, the original extracted sounding from DA10 is modified to ensure that the profile is balanced between the PGF, Coriolis, and frictional forces; the procedure employed for this modification will be described in the next subsection. With this configuration, the environmental wind profile (for both FWFRIC and EnvFRIC) remains more or less unchanged throughout our simulations. In addition, to keep the simulated storm quasi stationary near the center of the computational domain, we subtract the observed storm motion[1] of the 3 May 1999 central Oklahoma tornadic supercell ($u = 9.8\,\mathrm{m\,s^{-1}}$, $v = 7.8\,\mathrm{m\,s^{-1}}$) from the final environmental sounding. We call the storm-relative soundings before and after the force balance adjustment MAY3 and MAY3B, respectively.

Finally, convection in the model is triggered by an ellipsoidal thermal perturbation centered at $x = 40$ km, $y = 56$ km, and $z = 1.5$ km. The ellipsoid has a radius of 10 km in the horizontal and 1.5 km in the vertical, and the maximum potential temperature perturbation is 6 K at the center. This amplitude is necessary to obtain a sustained storm because of the very weak lid atop the planetary boundary layer (PBL) in our initial sounding, based on sensitivity tests.

b. Establishment of a balanced sounding and initialization of the storm environment

In three-dimensional (3D) idealized simulations, when the Coriolis force is included, the background environment should be in hydrostatic balance and (above the PBL) also in geostrophic balance. In the presence of vertical wind shear, then, there should be a thermal wind balance. This would imply the presence of a horizontal temperature gradient, unlike the horizontally homogeneous background environments traditionally used for single-sounding simulations. Furthermore, for simulations including the effect of surface drag, there is an additional frictional force within the PBL as a result of vertical momentum stress divergence. In the simplest case of constant eddy viscosity and a constant PGF within the PBL, the boundary layer wind would have a steady-state Ekman spiral profile. In this study, we wish to define a storm environment that is in geostrophic balance above the PBL and in a three-force balance (with friction added) within the PBL. When this force balance exists, the model state will remain steady over time in the absence of convective storm perturbations. In our case, we want to introduce a convective storm into this environment and study the effect of surface drag on the storm.

Setting up a 3D environment in thermal wind balance based on a single sounding is nontrivial, especially for a sounding with vertical wind shear that varies with height. A horizontal temperature gradient would need to be introduced into the background environment; for a geostrophic wind shear of $10\,\mathrm{m\,s^{-1}}$ over a 1-km vertical depth, this horizontal gradient would be about $3\,\mathrm{K\,(100\,km)^{-1}}$. Enforcing thermal wind balance in this way may introduce unrealistic structures into the vertical temperature profiles, complicating the analysis of the simulated supercell storm (e.g., when inflow air parcels from different parts of the model domain have different

[1] The storm motion was calculated manually using reflectivity data from the Oklahoma City, Oklahoma (KTLX), WSR-88D radar.

thermodynamic properties). Such issues were discussed at length in Skamarock et al. (1994, hereafter S94). For these reasons, we follow S94 and choose to neglect the horizontal temperature gradient associated with thermal wind balance, considering only the first-order geostrophic wind balance (and a three-force balance within the PBL). The horizontal pressure gradient is assumed to be in geostrophic balance with the environmental wind above the frictional boundary layer. The balance equations are as follows:

$$0 = -\frac{1}{\rho_s}\frac{\partial p_s}{\partial x} + f v_s, \tag{5}$$

$$0 = -\frac{1}{\rho_s}\frac{\partial p_s}{\partial y} - f u_s. \tag{6}$$

Here, subscript s denotes the base state that is in a hydrostatic and geostrophic balance. The supercell storm in our study has a spatial scale of only tens of kilometers, and we analyze our simulation over a period of 40 min, so the horizontal distance traveled by air parcels is relatively small (on the order of 10 km). The effects of neglecting the background horizontal temperature gradient should therefore be small for the short duration of our study: substantially smaller, in fact, than in the larger-scale mesoscale convective system (MCS) simulations of S94. In the present study, the base-state variables ρ_s, p_s, u_s, and v_s are defined by the original extracted sounding (MAY3) while the geostrophic horizontal pressure gradient is given by (5) and (6). MAY3 is assumed to be in geostrophic balance for the purpose of our adjustment procedure, despite the profile exhibiting a frictional PBL; the consequences of this will be discussed below.

In our simulations, surface drag is continuously acting on the environmental wind profile. For the background environment in these simulations to remain unchanged over time, a three-force balance within the PBL needs to be established. This is achieved by first running a 1D column version of ARPS for 48 h (long enough for geostrophic adjustment)[2], using the original extracted sounding MAY3 as the initial profile (this profile defines the base-state variables with subscript s). This 1D column simulation uses the same vertical grid and parameterization settings described in section 2a, and surface drag is turned on and applied to the full wind.

When the 1D solution reaches a steady state, the following equations are satisfied:

[2] The wind profile in the 1D column simulation reaches a quasi-steady state after 12 h, but integration is carried out to 48 h to ensure robustness.

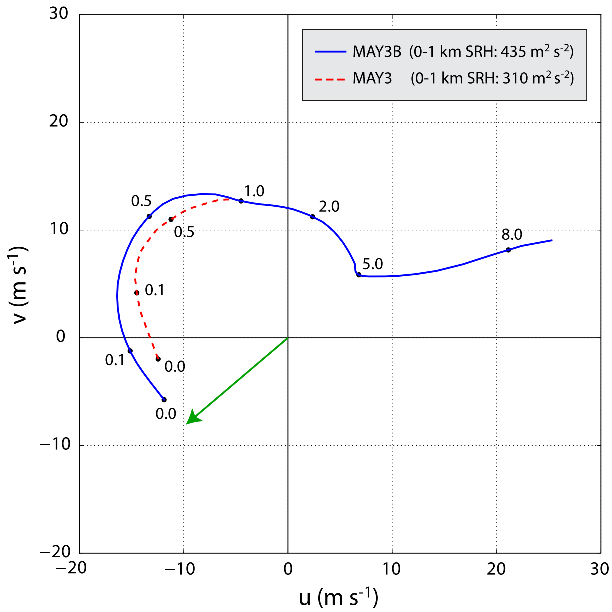

FIG. 1. Wind hodograph for storm-relative soundings MAY3B (solid blue) and MAY3 (dashed red) up to 8 km AGL. Numerical values along the hodograph denote the height AGL (km) at which the nearest black dot is valid. Above 1 km AGL, the hodographs are qualitatively identical, so MAY3 is omitted for clarity. The green arrow represents the ground-motion vector (i.e., the vector that was added to the original extracted wind profile to obtain a quasi-stationary storm in our simulations). The 0–1-km AGL storm-relative helicity is provided for each hodograph in the legend.

$$0 = -\frac{1}{\rho_s}\frac{\partial p_s}{\partial x} + f(v_s + v') + F_x(u_s + u'), \tag{7}$$

$$0 = -\frac{1}{\rho_s}\frac{\partial p_s}{\partial y} - f(u_s + u') + F_y(v_s + v'), \tag{8}$$

where the prime terms are deviations from the original sounding MAY3, and F represents the frictional terms. The term $F(\cdot)$ denotes that surface drag is calculated from the quantity inside the parentheses. The final wind profile 48 h into the 1D simulation, given by $\overline{u} = u_s + u'$, $\overline{v} = v_s + v'$, is taken as the profile for MAY3B, which is used to initialize our 3D simulations. As mentioned earlier, the storm motion has been subtracted from the wind profile in both MAY3 and MAY3B, but the ground-relative wind speed is always used in the calculation of surface drag. We note that, in our simulations, the Coriolis force is actually applied only to deviations from MAY3, because of the assumed balanced between the base-state horizontal PGF and the base-state geostrophic wind, as given by (5) and (6).

Figure 1 shows the storm-relative hodographs for MAY3 and MAY3B. Vertical wind shear is stronger within the lowest 1 km AGL in MAY3B, resulting in a

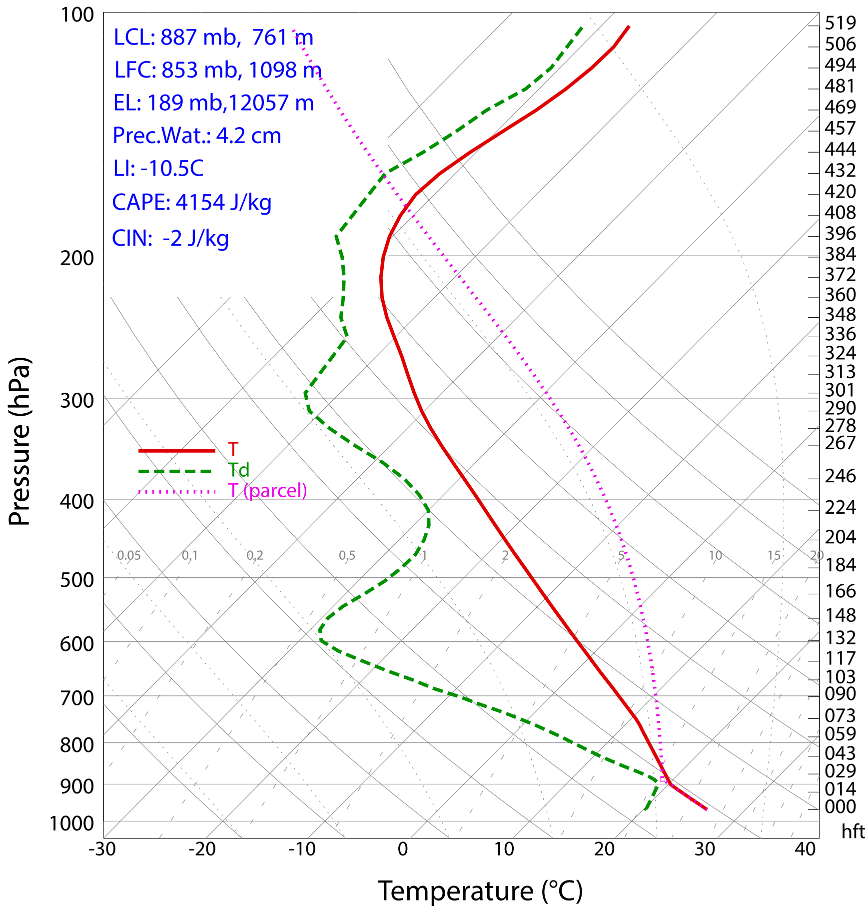

FIG. 2. Skew T–log$p$ plot for sounding MAY3B. The environmental temperature and mixing ratio are denoted by the solid red and dashed green lines, respectively. The temperature for an ascending surface-based parcel is denoted by the pink dotted line.

0–1-km-AGL storm-relative helicity (SRH) approximately 40% larger than in MAY3. Although we assume MAY3 is in geostrophic balance when we initialize the 1D adjustment simulation, DA10's simulation from which MAY3 is extracted actually did include surface drag (using a stability-dependent drag coefficient whose value at the sounding location was smaller than our constant value of $C_d = 0.01$). This yields somewhat exaggerated near-ground wind shear in MAY3B, compared to starting the 1D simulation with the true geostrophic wind profile (which is not precisely known but contains much less shear in the lower levels than MAY3). Sensitivity testing suggests that about half of the difference in 0–1-km SRH between MAY3 and MAY3B is due to this geostrophic assumption, with the remaining difference being attributable to the larger drag coefficient in our simulations.

Although MAY3B exhibits modestly exaggerated 0–1-km SRH, it nonetheless represents a profile in three-force balance between the horizontal PGF, Coriolis, and frictional forces in the model. To verify that this force balance holds in the 3D simulations, a version of experiment FWFRIC without an initial thermal bubble is integrated for 2400 s; the final kinematic profile throughout the domain is found to be virtually unchanged from the initial profile (not shown).

Note that, during the 1D column run, the moisture and temperature profiles from MAY3 are also modified somewhat as the turbulence scheme operates on a grid with a higher vertical resolution than that used in DA10. This is a consequence of the 1.5 TKE formulation specifying mixing length as a function of grid spacing (Moeng and Wyngaard 1988). The resulting profile exhibits a relatively realistic, well-mixed boundary layer (Fig. 2). This modified thermodynamic profile is used in MAY3B, allowing the background environment to remain virtually unchanged during the 3D simulations.

3. Simulation results

a. *Overview and qualitative comparison of experiments*

This section compares and contrasts experiments FWFRIC and EnvFRIC. In both cases deep convection develops rapidly during the first 600 s from the initial thermal bubble at (x = 40 km, y = 56 km). By 600 s, convergence has developed at the lowest model level in response to the strong updraft (Figs. 3a,e). The convergence continues to strengthen underneath the main updraft and along a north–south-oriented boundary over the next 7 min (Figs. 3b,f) and beyond.

The low-level wind pattern in FWFRIC and EnvFRIC is qualitatively similar through 600 s. More noticeable differences start to appear around 700–900 s at the lowest model level (10 m AGL), when the flow directed toward the convergence boundary in EnvFRIC grows significantly stronger than in FWFRIC, reflecting the retarding effect of surface drag on convection-induced winds in the latter. This trend continues through 1200 s. Despite the noticeable difference between the two experiments, the general pattern of the low-level flow is still qualitatively similar at 1020 s (Figs. 3b,f).

By 1380 s, the first convective precipitation has reached the ground in both experiments. In FWFRIC, the strongest surface convergence is concentrated primarily in a small, arcing zone at the northern tip of the convergence boundary; the convergence boundary itself is also thinner, with a stronger maximum convergence magnitude (Fig. 3c). By contrast, the surface convergence boundary in EnvFRIC appears more diffuse, albeit with some arcing at the northern end (Fig. 3g). The convergence boundary is reminiscent of a rear-flank gust front associated with a classical RFD (Lemon and Doswell 1979) in both extent and storm-relative position. However, in the absence of significant precipitation or a cold pool, we do not consider the boundary a rear-flank gust front. While details of this boundary's formation are beyond the scope of this paper, we speculate its development to be a result of interaction between the low-level storm-relative vertically sheared environmental flow and the storm-induced flow converging toward the center underneath the developing updraft. The vertical wind shear in the environment is likely a key factor.[3]

Between 1380 and 1500 s, differences between low-level winds in the two experiments continue to increase near the area of maximum surface convergence (Figs. 3d,h). In particular, the arcing boundary in FWFRIC becomes more curved than in EnvFRIC, with a thinner and stronger convergence zone. To examine the evolution of this boundary more closely, a zoomed plan view of horizontal convergence, perturbation pressure, and ground-relative wind is presented in Fig. 4. At 1260 s, the difference between experiments in boundary curvature is still relatively small (Figs. 4a,c), although the difference in the width of convergence zone is significant. The most notable difference in the wind field is found immediately to the west of the boundary near (x = 36 km, y = 63 km), where flow in FWFRIC has a prominent northward-directed component, which is absent in EnvFRIC. Immediately west of the boundary, flow in FWFRIC is directed northeastward, approximately normal to the boundary; flow in EnvFRIC is directed eastward, meeting the boundary at a substantially smaller angle. This enhances the surface convergence in FWFRIC and promotes the development of curvature along the northern segment of the boundary. By contrast, the northern segment of the boundary in EnvFRIC does not bend back to the west as much, as flow west of the boundary retains a strong westerly component. By 1380 s, the arcing boundary in FWFRIC has become more curved (Fig. 4b); a secondary convergence zone has developed near (x = 36 km, y = 64 km) to the west of the primary zone, creating a horseshoe-shaped convergence boundary. No clearly defined secondary convergence boundary forms in EnvFRIC, and the main boundary remains comparatively straight and broad (Fig. 4d).

Time–height cross sections of domainwide maximum updraft speed show more dramatic differences between the two experiments at later times (Fig. 5). The experiments are qualitatively similar in terms of domainwide maximum updraft until 1300 s, when a stronger updraft develops around 1.5 km AGL in FWFRIC. This stronger updraft quickly expands in vertical extent both upward and downward, exceeding 30 m s^{-1} at 250 m AGL in the developing tornado by 1500 s. Horizontal cross sections (not shown) reveal that the strong updraft in FWFRIC is positioned almost directly above the strongest surface convergence.

The time–height vertical sections for domainwide maximum vertical vorticity ζ (Fig. 6) also show that the two experiments are qualitatively similar until around 1200 s. Around that time, enhanced cyclonic ζ develops in FWFRIC between 500 and 1000 m AGL and expands in vertical extent after 1350 s. Coincident with the development of strong surface convergence and low-level updraft, a concentrated area of cyclonic vertical vorticity develops at the lowest grid level (10 m

[3] If the environmental wind were constant throughout the depth of the atmosphere, the low-level flow would remain symmetric about the convergence center underneath the updraft (in the absence of surface drag).

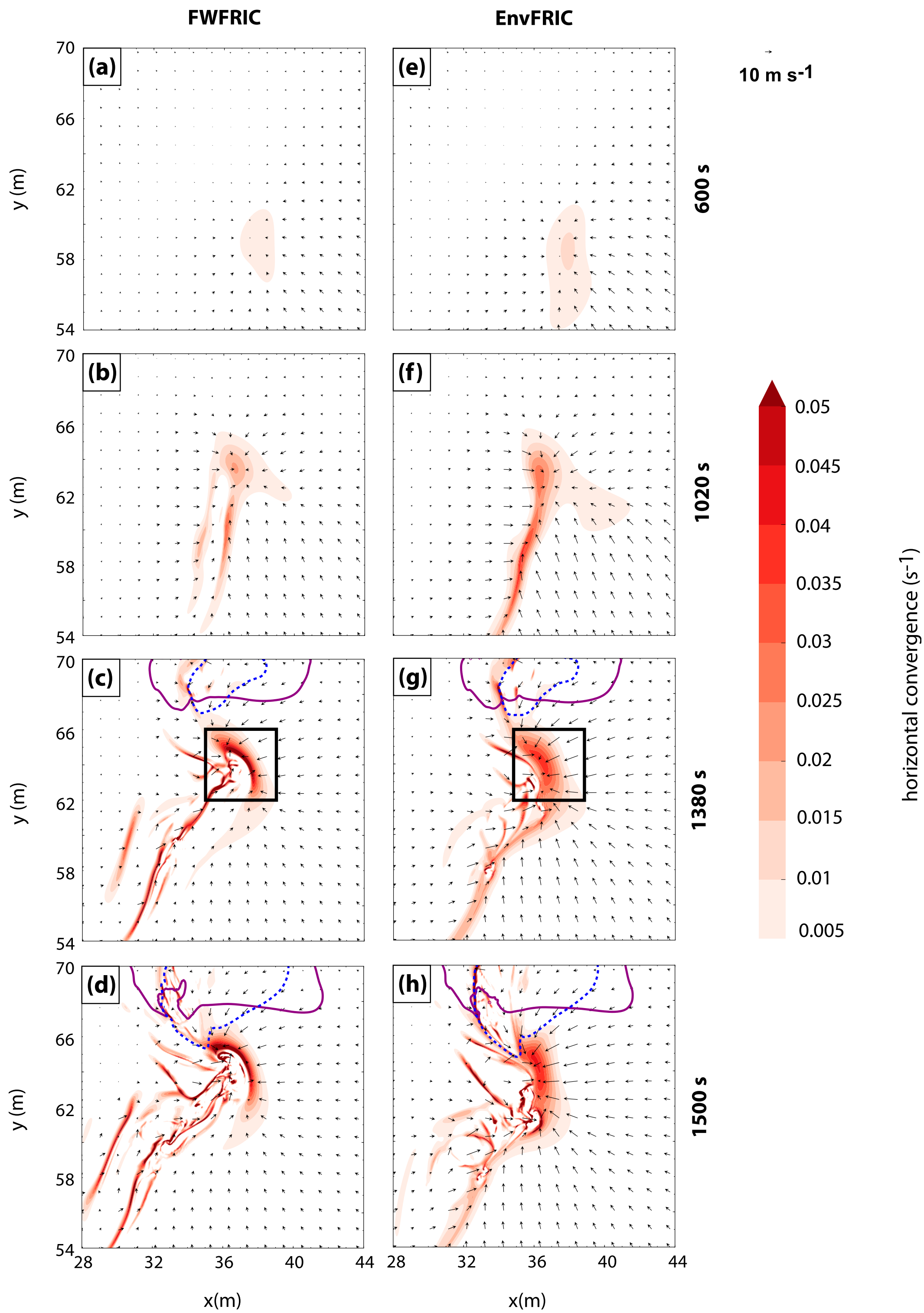

FIG. 3. Horizontal convergence (shaded), −1-K perturbation potential temperature contour (dashed blue), 0.3 g kg^{-1} rainwater mixing ratio contour (solid purple), and ground-relative wind vectors at 10 m AGL for FWFRIC at (a) 600, (b) 1020, (c) 1380, and (d) 1500 s and for EnvFRIC at (e) 600, (f) 1020, (g) 1380, and (h) 1500 s. The storm motion is added to the model wind field to obtain ground-relative wind vectors. In (c) and (g), the black box denotes the zoomed region plotted in Fig. 4.

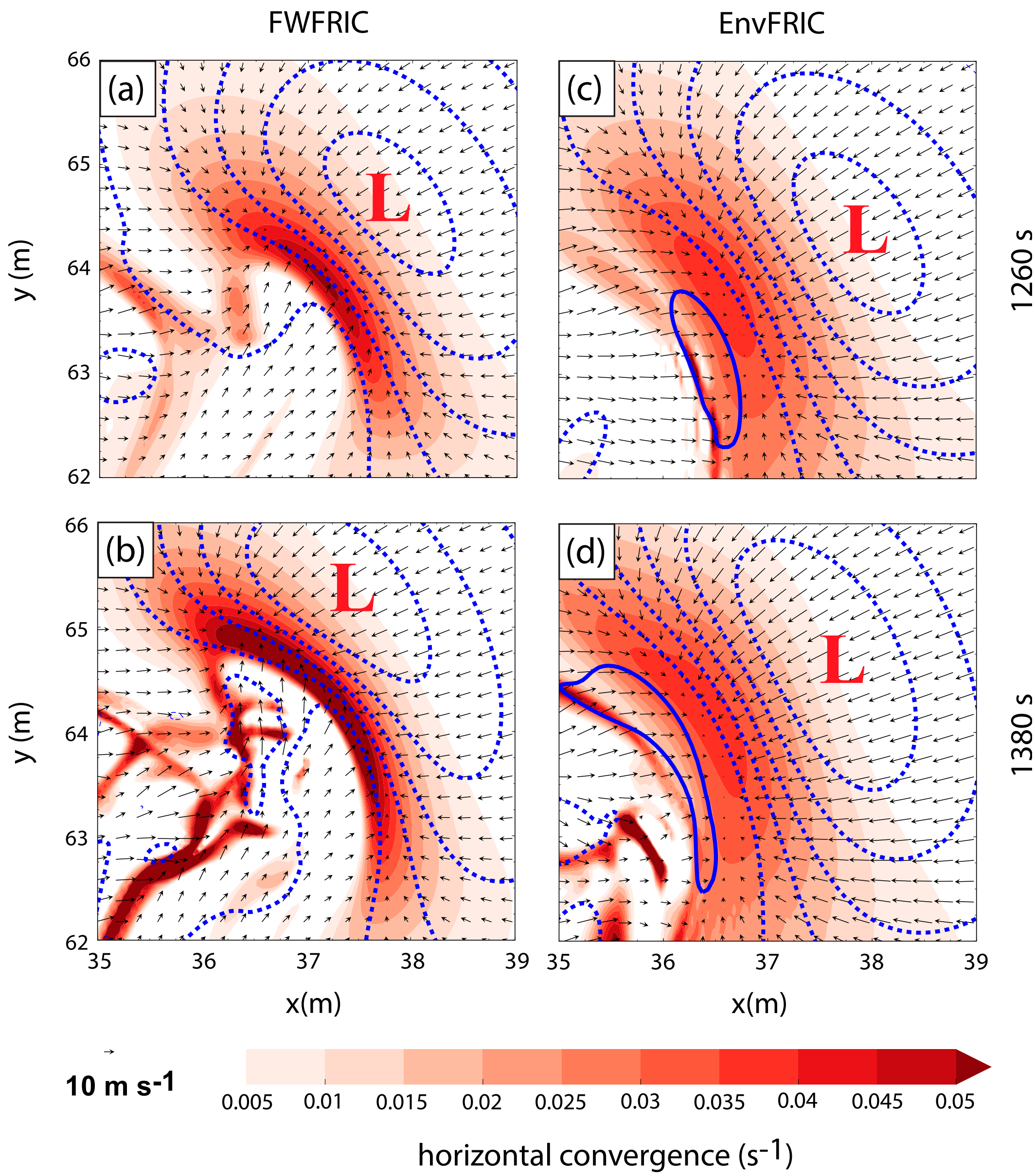

FIG. 4. Horizontal convergence (shaded), perturbation pressure (blue contours; thick line is 0 hPa and negative values at 1-hPa intervals dotted), and ground-relative wind vectors at 10 m AGL for FWFRIC at (a) 1260 and (b) 1380 s and for EnvFRIC at (c) 1260 and (d) 1380 s. Red L in each panel denotes local pressure minimum.

AGL) in FWFRIC by 1350 s near ($x = 37$ km, $y = 63$ km) (Fig. 7a). This strong vorticity center is considered a pretornadic vortex (PTV) until 1500 s. Shortly before 1500 s, very large vertical vorticity exceeding 1 s^{-1} develops at the surface, which expands upward to 500 m AGL quickly. By this time, the surface vortex has reached tornado intensity based on our criteria that the maximum near surface horizontal wind speed V_h exceeds the [enhanced Fujita (EF) scale] EF0 threshold (29 m s^{-1}), and ζ exceeds 0.3 s^{-1}. The vortex maintains tornado intensity through 2100 s and beyond (Fig. 6). By contrast, while the largest ζ is found near the ground in EnvFRIC near 1800 s, it never exceeds 1 s^{-1}. Horizontal cross sections near the ground in EnvFRIC reveal that only transient areas of $\zeta > 0.3$ s^{-1} occur along the convergence zone during the same time period (not shown). Eventually, a shallow vortex (extending upward only to about 1 km AGL) forms around 1800 s that persists for about 60 s. However, wind speeds in this vortex do not exceed the EF0 threshold, so tornadogenesis does not occur in EnvFRIC.

The tornado in FWFRIC reaches its peak intensity around 1620–1680 s (Fig. 7c), during which time the

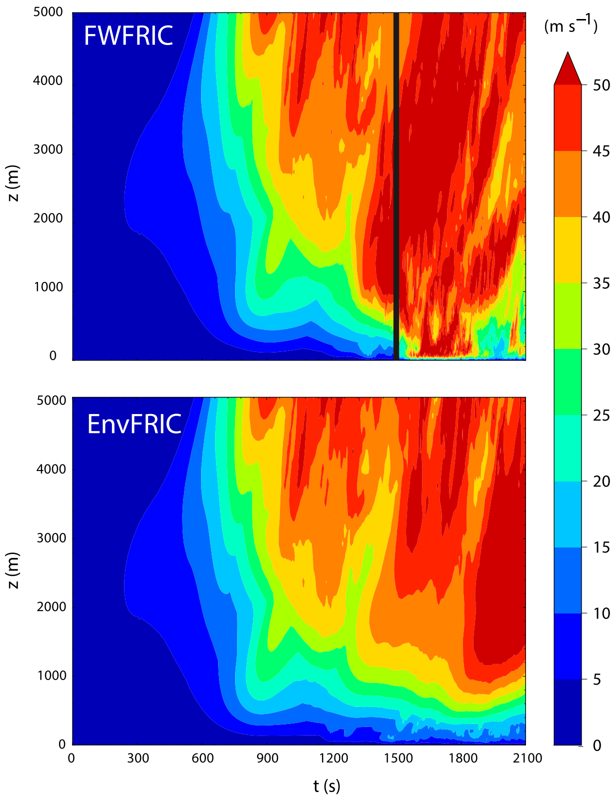

FIG. 5. Time–height section of domainwide maximum updraft for (top) FWFRIC and (bottom) EnvFRIC, valid from 0 to 2100 s. The heavy black vertical line in FWFRIC denotes the time of tornadogenesis (1500 s).

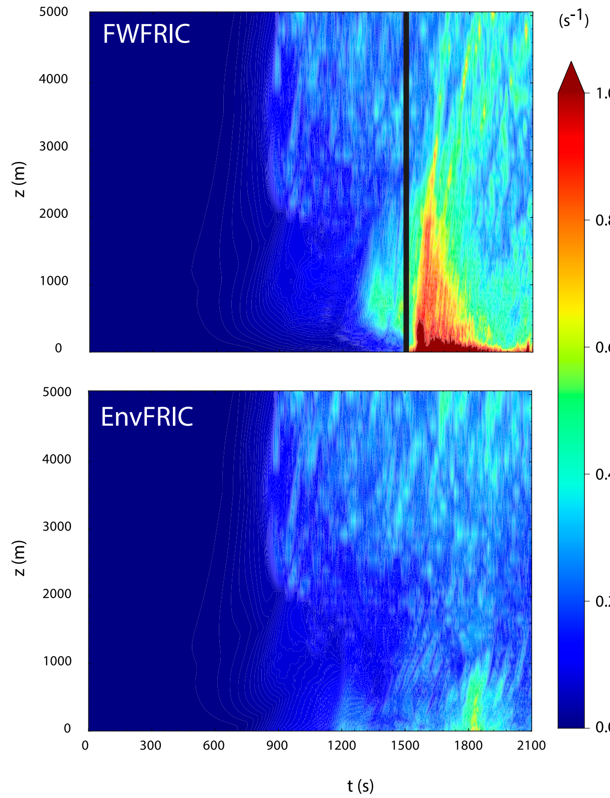

FIG. 6. As in Fig. 5, but for domainwide maximum vertical vorticity.

maximum V_h near the ground approaches 100 m s^{-1}, and ζ at the lowest grid level AGL briefly exceeds 2 s^{-1}. A vertical cross section through the tornado at 1620 s reveals that it extends vertically to 2–3 km AGL, tilting from south-southeast to north-northwest with height (Fig. 8a). Figure 8a also shows that, by this time, a two-celled structure has developed in the tornado; at its center exists a downdraft that is strongest below 500 m AGL, and the downdraft is also found between 1300 and 1900 m AGL. The downdraft is consistent with the large negative pressure perturbation near the surface at the vortex center, creating a large negative downward PGF (Fig. 8b). The low-level downdraft is surrounded by strong updraft, which exceeds 35 m s^{-1} at about 100 m AGL on the north-northwest side of the vortex. The maximum vorticity is found at the center of the vortex, consistent with the structure seen in the horizontal cross section in Fig. 7c. At later times, an annular structure develops in the vorticity field where maximum vertical vorticity is found within a ring surrounding the center (Fig. 7d). Horizontal cross sections at and above 1 km AGL (not shown) indicate that the tornado is positioned near the center of the broader low-level mesocyclone.

b. Trajectory analysis of PTV/tornado in FWFRIC

We will focus on experiment FWFRIC for the remainder of section 3 because it produced a tornado. Parcel trajectories are initialized in the vortex for various times preceding, during, and after tornadogenesis. These trajectories are numerically integrated backward in time for 900 s using the fourth-order Runge–Kutta method from model output wind fields (at an interval of 2 s, with 0.25 s subintervals to which the wind field is interpolated linearly in time between data files) to trace the source of vorticity feeding the vortex in the low-levels. Of particular interest is the evolution of the Lagrangian source terms for both vertical and horizontal vorticity components as parcels approach and enter the vortex.

D14 discussed at length the challenges associated with treatment of trajectories passing below the lowest scalar variable level (which is half a grid interval above ground: 10 m AGL for the present study, and 50 m AGL for the simulations of D14), particularly in the context of vorticity budget analyses. They discussed two possible

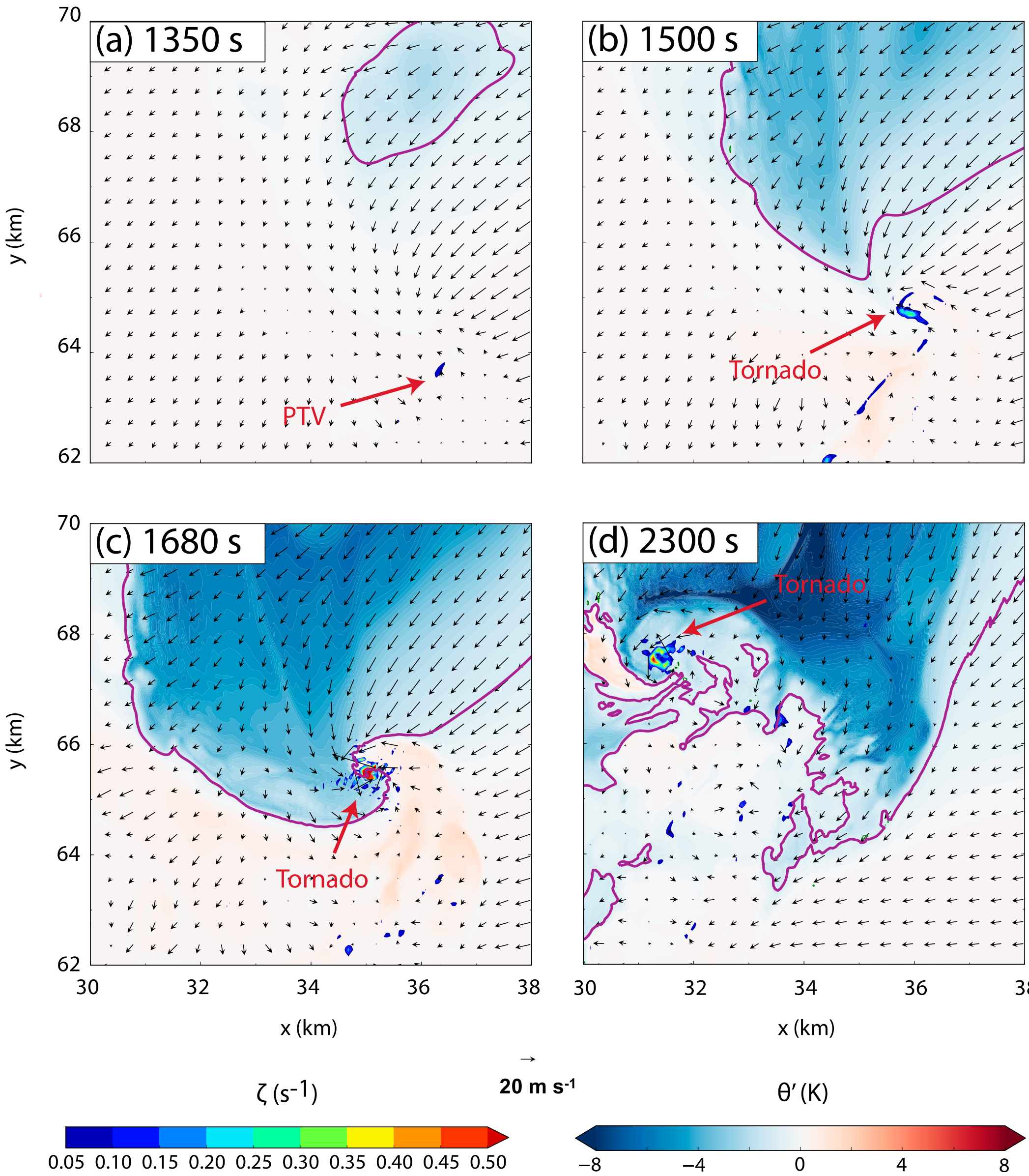

FIG. 7. Evolution of PTV and subsequent tornado in FWFRIC at 10 m AGL at (a) 1350, (b) 1500, (c) 1680, and (d) 2300 s. Perturbation potential temperature is shaded, with the −1-K contour highlighted in purple. Vertical vorticity is shaded in the foreground, where $\zeta > 0.05\ \mathrm{s}^{-1}$. Ground-relative wind vectors are plotted. The location of the PTV/tornado is denoted in each panel.

treatments for parcels in this region for free-slip lower boundary simulations: 1) assuming no vertical gradient for horizontal velocity below the lowest scalar level and 2) extrapolating horizontal velocity downward from the lowest scalar level to ground level. Both methods can result in a dynamical inconsistency between the vorticity field and horizontal velocity field and are therefore problematic in the context of Lagrangian vorticity budgets. In semislip simulations, such as those in the present study, vorticity is similarly ill defined in this region, since a zero-gradient condition is assumed for the horizontal wind components across the lower boundary. Indeed, in the present study, agreement between Lagrangian and interpolated[4] values of the horizontal vorticity components is poor during times when parcels

[4] In the context of trajectories in this study, "interpolated" refers to vorticity values interpolated directly from the model grid to the trajectory location; "Lagrangian" refers to values obtained through time integration of vorticity source terms along the trajectory (which themselves are also interpolated from the model grid).

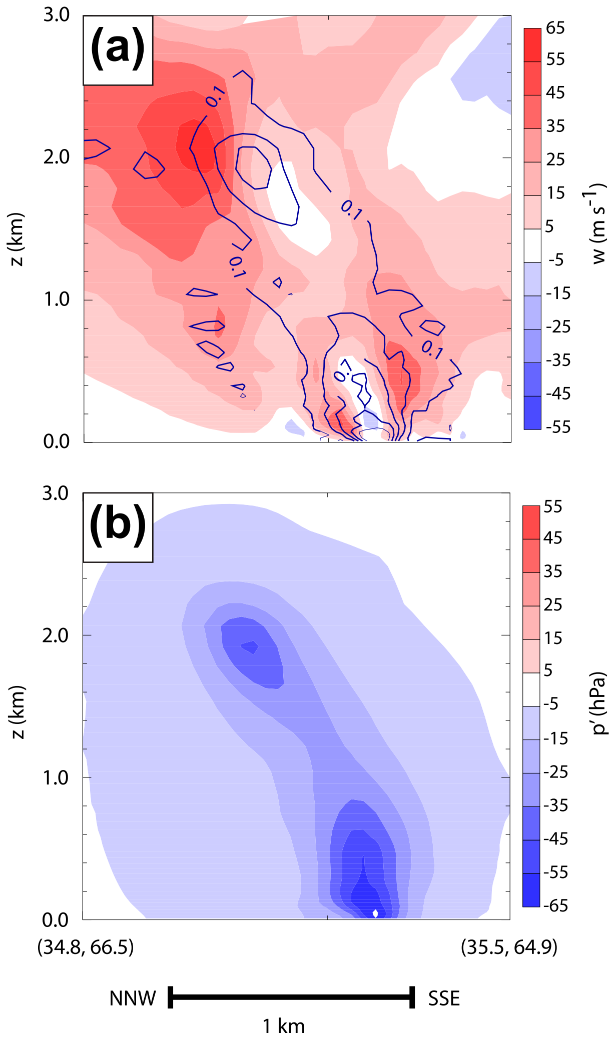

FIG. 8. Vertical cross section through the tornado in FWFRIC at 1620 s of (a) vertical velocity (shaded) and vertical vorticity (contour; s^{-1}) and (b) perturbation pressure (shaded). The cross section is along a vertical plane extending from (x = 34.8 km, y = 66.5 km) at the north-northwest end to (x = 35.5 km, y = 64.9 km) at the south-southeast end.

descend below the lowest scalar level (10 m AGL). Consequently, we require that a parcel remains above 10 m AGL at all times during the backward integration for it to be selected for quantitative analyses. Because of this, we initialize our backward trajectories at either 400 or 600 m AGL within the vortex (where $\zeta \geq 0.1\,s^{-1}$), since trajectories initialized at lower heights almost invariably originate from below 10 m AGL. Still, most of these trajectories get very close to the lowest scalar level (10 m AGL) on their approach to the vortex.

Figure 9a presents horizontal paths of trajectories entering the PTV at 400 m AGL at 1440 s. Parcels are found to originate almost exclusively from northeast of the vortex and below 100 m AGL, translating horizontally within this layer until ascending rapidly into the PTV at the end of the integration period. This distribution strongly favoring inflow trajectories from northeast of the vortex remains dominant at the time of tornadogenesis (1500 s, Fig. 9b) and even when the tornado is near its peak intensity (1560 s, Fig. 9c).

Dahl et al. (2012, hereafter D12) investigated the accuracies of backward parcel trajectories that entered a low-level mesocyclone in two supercell simulations (using 250-m horizontal grid spacing, and ~100-m vertical spacing near the ground). It was found that, as the time interval of the model velocity data used to calculate the trajectories increases, more backward trajectories enter the mesocyclone directly from the inflow without going through the downdraft region, a result that appeared to be erroneous in their simulations. The amplification of trajectory calculation errors initially created near the vortex (where flow curvature and velocity time tendencies are large) is believed to be the primary reason. In the present study, the model velocity data interval is only 2 s, but compared to the time it takes for a near-vortex parcel to travel one grid interval (about 0.5 s) it is still relatively large.

Because inflow trajectories are dominant in the present study, in order to test their accuracy, test trajectories are initialized in a grid pattern covering the area of origin suggested by the backward trajectories, then integrated forward in time. Note that these forward trajectories are integrated using the same 2-s data interval as the backward trajectories. D12 suggests that forward trajectories are inherently less prone to error amplification in regions of convergent flow, such as those flowing toward a tornado. Several of these forward test trajectories enter the tornado (not shown), and nearly all follow qualitatively similar paths toward the low-level mesocyclone when compared with the backward trajectories, increasing our confidence that the backward trajectories we analyze in this section are qualitatively reasonable. The thermodynamic and kinematic structure of the supercell in the present simulation differs markedly from the structure in D12; tornadogenesis occurs much earlier in the storm's evolution herein before a precipitation-driven downdraft is well established. Thus, it is plausible that inflow trajectories are dominant in the present study even if they are less prevalent in storms with well-established or stronger cool outflow, as in the case of D12. Indeed, Dawson et al. (2015) also found an inflow-dominant distribution of vortex-entering trajectories in a real-data simulation of the same 3 May 1999 case used as the basis for our sounding. Still, based on the results of D12 and given the rapidly evolving flow, we are less confident in the accuracy of the minority of our trajectories that enter along

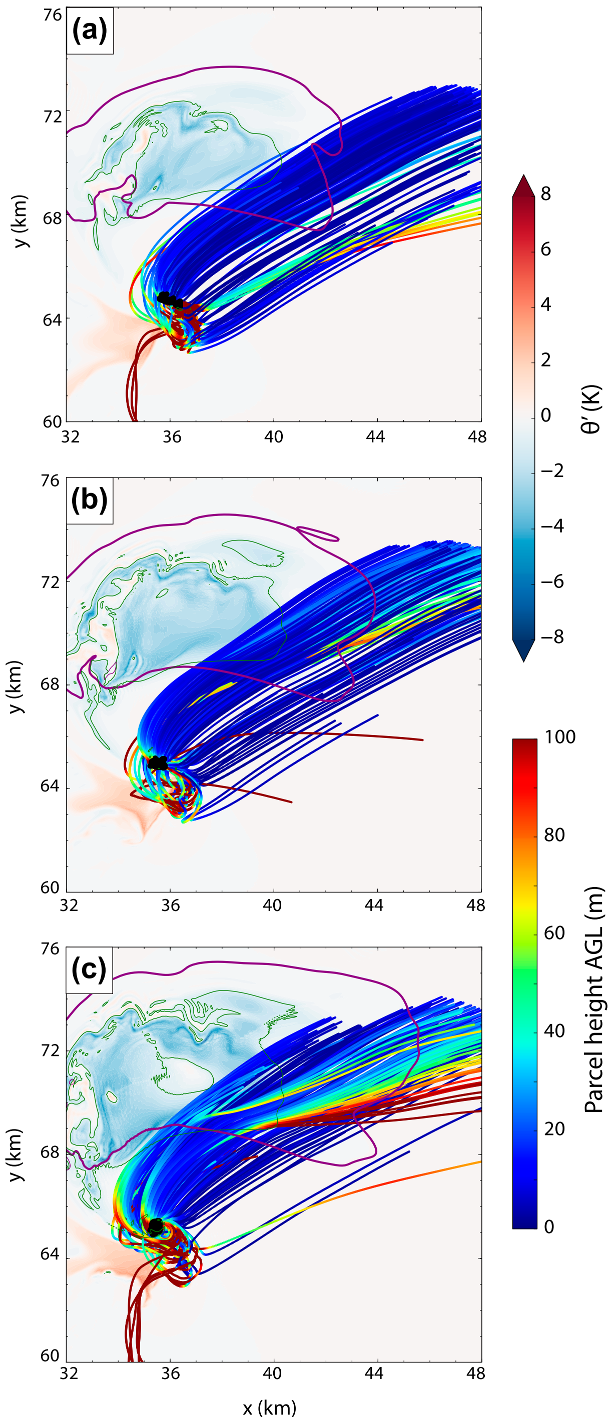

FIG. 9. Horizontal projection of trajectories initialized on a 1 km × 1 km square grid centered on the PTV/tornado at 400 m AGL at (a) 1440, (b) 1500, and (c) 1560 s. Only trajectories with a final vertical vorticity value of $\zeta \geq 0.1\,\mathrm{s}^{-1}$ are shown. The trajectories were integrated 900 s backward in time and are color-coded by parcel height along the path, with a black dot denoting their final position in the PTV/tornado. For context, these trajectories are overlaid atop a horizontal cross section (valid at the same time as the trajectory initialization in each panel) at 400 m AGL of perturbation potential temperature (shaded, with a green contour for −1 K) and the 0.3 g kg^{-1} rainwater mixing ratio contour (heavy purple contour).

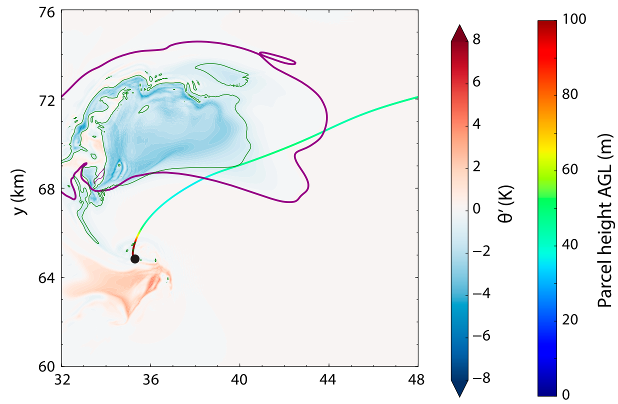

FIG. 10. As in Fig. 9b, but only the RP trajectory (which enters the tornado at 1500 s) is shown.

straight paths from due east of the vortex (most prominent at 1440 s) and will not include them in the analysis which follows.

A representative parcel (RP), which enters the tornado at 1500 s, is chosen for the purpose of a detailed vorticity budget analysis. The horizontal path of the RP (Fig. 10) qualitatively resembles most of the tornado-entering trajectories valid at the same time in Fig. 9b. It originates from a height of approximately 50 m AGL at 600 s, remaining within ±20 m of that height throughout its approach until it begins ascending into the tornado after 1400 s.

Of chief concern for the RP is the evolution of its vorticity components as it approaches the vortex, and particularly of the source[5] terms responsible for any significant changes in the magnitude or orientation of the vorticity. Figure 11a presents an along-trajectory ζ time series for the RP between 1140 and 1470 s, while Fig. 11b depicts ζ source terms over the same period. The fact that the vorticity obtained by integrating the vorticity equation with its source terms along the trajectory agrees well with the vorticity interpolated to the trajectory from the model fields (Fig. 11a) suggests that both the trajectory calculation and vorticity integration are very accurate for the RP.

It is apparent that, after 1450 s, stretching is the dominant source of cyclonic ζ generation as the parcel ascends rapidly, leading the RP to acquire tornado-strength vorticity within the following minute. Because stretching can only act on existing vertical vorticity, the

[5] We use "source term" in this paper to refer to any term that appears on the right-hand side of the prognostic equation for a vorticity component: that is, of (9) and (10). Some of these terms, such as the stretching and tilting terms, are not true sources of vorticity in the sense of new vorticity production, but represent the transport or reorientation of existing vorticity.

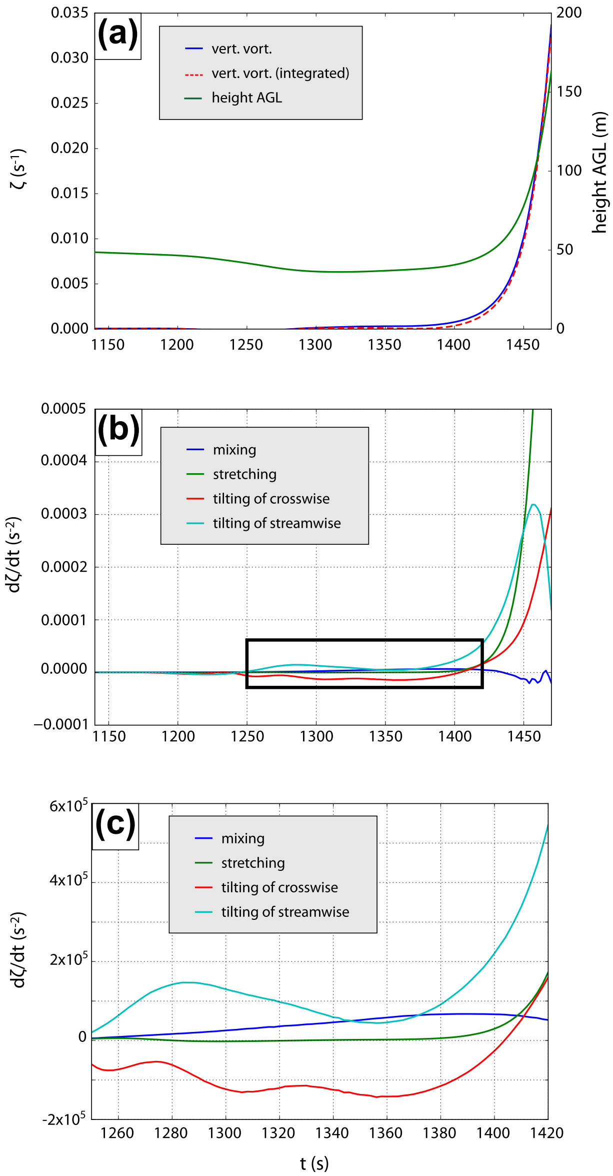

FIG. 11. Time series from 1140 to 1470 s along the representative parcel trajectory shown in Fig. 10 of (a) parcel height AGL, model-predicted vertical vorticity (interpolated to the parcel locations), and vertical vorticity integrated from generation terms and (b) vertical vorticity source terms. (c) A zoomed time series of source terms from 1250 to 1420 s. The period plotted in (c) is denoted by the black box in (b).

critical question becomes the following: Which term(s) produced low-level cyclonic ζ prior to this amplification by stretching? Before stretching becomes dominant around 1450 s, tilting of streamwise[6] horizontal vorticity into the vertical is responsible for most of the positive ζ generation (Fig. 11b). By contrast, tilting of crosswise horizontal vorticity into the vertical has a negative contribution for much of this period before becoming weakly positive after 1380 s (Fig. 11c).

Because tilting of streamwise vorticity is the primary source of positive ζ for the RP, we want to identify the source of this streamwise vorticity. The prognostic equations for the streamwise horizontal vorticity ω_s and crosswise horizontal vorticity ω_c are, respectively,

$$\frac{D\omega_s}{Dt} = \boldsymbol{\omega}\cdot\nabla V_h + \frac{\partial B}{\partial n} + \frac{1}{\rho}\left(\frac{\partial F_z}{\partial n} - \frac{\partial F_n}{\partial z} - F_s\frac{\partial \psi}{\partial z}\right) + \omega_{hc}\frac{D\psi}{Dt}, \quad (9)$$

$$\frac{D\omega_c}{Dt} = \boldsymbol{\omega}\cdot V_h\nabla\psi - \frac{\partial B}{\partial s} + \frac{1}{\rho}\left(\frac{\partial F_s}{\partial z} - \frac{\partial F_z}{\partial s} - F_n\frac{\partial \psi}{\partial z}\right) - \omega_{hs}\frac{D\psi}{Dt}, \quad (10)$$

where $\boldsymbol{\omega}$ is the 3D relative vorticity vector; V_h is the horizontal wind magnitude; $\psi = \tan^{-1}(v/u)$ is the horizontal wind direction; B is the buoyancy (including the weight of hydrometeors); and F_s, F_n, and F_z are, respectively, the horizontal streamwise, horizontal crosswise, and vertical components of the frictional force.[7] In both (9) and (10), the right-hand side (rhs) terms represent, in order, generation by the following: stretching and tilting, baroclinity, friction/mixing, and exchange of vorticity between the streamwise and crosswise directions. Equations (9) and (10) are the same as those given in Mashiko et al. (2009) and S14, except that the last term involving $\partial\psi/\partial z$ in the frictional term in both equations was missing in their papers. In the case of S14, this was simply an error in the written equations; the calculations used for vorticity budgets employed the correct formulation, and the same code was also used in the present study. Note that we neglect the effects of Coriolis in (9) and (10), since the time scale to produce tornado-strength vorticity from Earth's vorticity is much longer than our trajectory calculations (e.g., Davies-Jones 2015).

Time series of total (3D), crosswise horizontal, and streamwise horizontal vorticity for the RP between 1140 and 1470 s are presented in Fig. 12a. Initially, the magnitude of the streamwise component is considerably larger than the crosswise component, owing to the large, clockwise-curving hodograph of the background

[6] All references to "streamwise" and "crosswise" hereinafter are in the storm-relative framework (i.e., streamwise is considered to be in the direction of the local model-predicted wind).

[7] Note that the frictional force represents the combined effects of numerical diffusion and subgrid-scale turbulence mixing. The frictional force is actually the result of turbulence momentum flux or stress tensor divergences, and the surface drag enters the governing equations as the lower boundary condition of the vertical turbulence flux for momentum; see section 2b for further details.

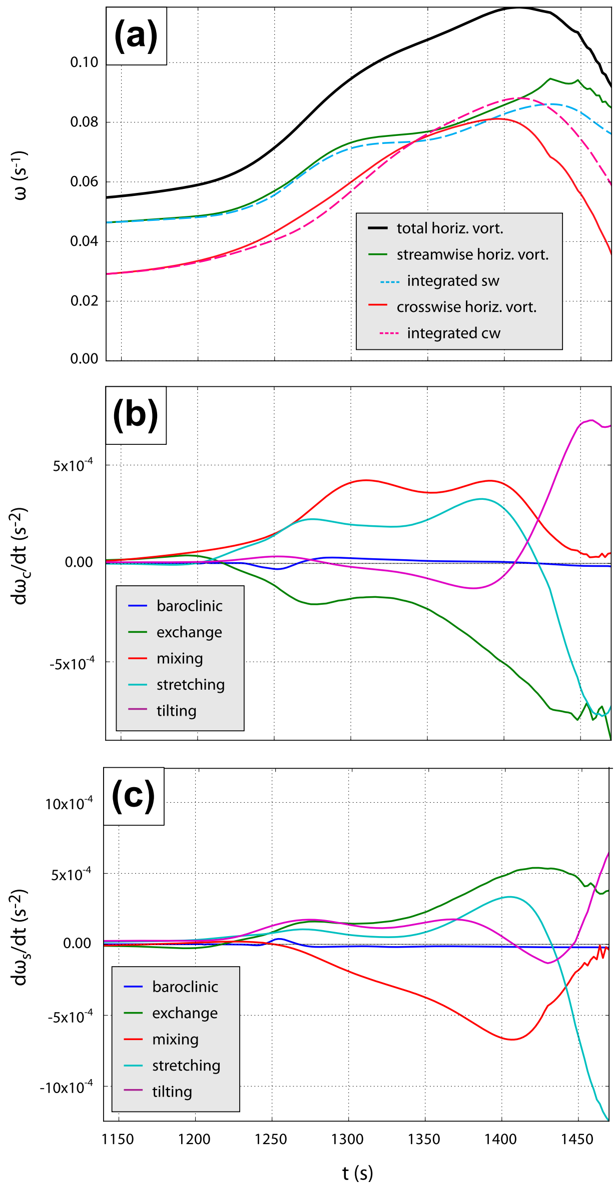

FIG. 12. Time series for the representative parcel trajectory from 1140 to 1470 s of (a) total horizontal vorticity, along with its streamwise and crosswise components (and their integrated values from source terms of the vorticity equations as dashed lines); (b) horizontal crosswise vorticity source terms; and (c) horizontal streamwise vorticity source terms.

environment (see Fig. 1). Between 1140 and 1400 s, the total horizontal vorticity magnitude for the RP approximately doubles, and the parcel remains near 50 m AGL. During this preascent period, the crosswise component of horizontal vorticity experiences a larger relative increase than the streamwise component. A time series of the horizontal crosswise vorticity source terms for the RP (Fig. 12b) reveals that the frictional mixing term is responsible for much of this increase, with stretching playing a secondary role (the flow accelerates horizontally before it gets very close to the convergence zone). The magnitude of crosswise mixing generation is largest between 1300 and 1400 s, then starts to decrease after 1400 s; partially as a result, the crosswise horizontal vorticity also begins to decrease after 1400 s. The loss of positive crosswise to streamwise vorticity through the exchange term is significant from 1220 s onward and becomes much larger after 1400 s.

Figure 12c shows that exchange of crosswise vorticity into the streamwise direction is the dominant source of positive generation for horizontal streamwise vorticity. The exchange term in Fig. 12c is maximized between 1400 and 1450 s, after the horizontal crosswise vorticity has reached its peak value, highlighting that horizontal vorticity initially created in the crosswise direction is converted to streamwise vorticity (especially when the parcel is close to the incipient tornado). Baroclinic generation of horizontal vorticity is negligible throughout the RP's approach.

Given that the RP is located around 30–50 m AGL (near the second grid level AGL) while the mixing term for crosswise vorticity is relatively large (Fig. 12b), surface drag should be regarded as the dominant physical mechanism by which the mixing term generates crosswise horizontal vorticity (vorticity pointing to the left of the flow). Indeed, in the presence of surface drag, accelerating near-ground flow must experience negative stress from below that generates positive crosswise vorticity. Thus, a clear picture emerges for how horizontal vorticity becomes substantially larger than its environmental value and ultimately is tilted into the vertical.

First, horizontal crosswise vorticity is generated by surface drag as the parcels originating from the inflow region accelerate near the ground and flow into the low-level convergence center along cyclonically curved paths (c.f. Fig. 10). Along the paths and especially as the parcels get close to the convergence center, a significant portion of this crosswise vorticity is exchanged into the streamwise direction. This exchange appears to be an example of the so-called "riverbend effect" described in Davies-Jones et al. (2001), whereby crosswise vorticity is converted to streamwise vorticity within cyclonically curved flow (Fig. 13). Finally, as the parcels enter the convergence zone, horizontal streamwise vorticity is tilted into the vertical, and the vertical vorticity is rapidly amplified through stretching as the parcels ascend (Fig. 11a). Very similar processes were found in the simulation of a real supercell storm in S14.

To ensure the representativeness of the vorticity budgets for the RP, vorticity source terms are calculated for a large sample of vortex-entering parcels; specifically, we analyze a subset (n = 442 for 1440 s, n = 694 for 1500 s, and n = 469 for 1560 s) of the parcels whose paths are

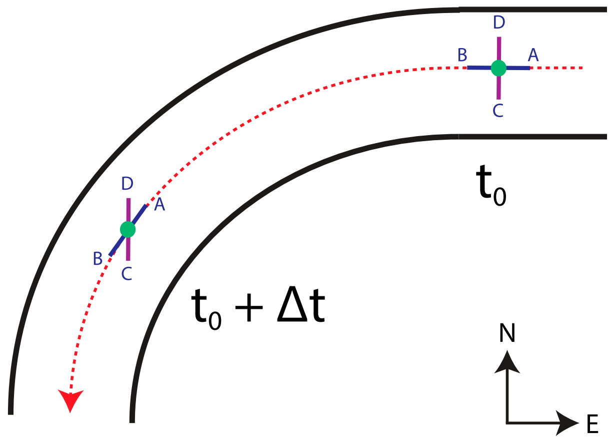

FIG. 13. Diagram of flow around a riverbend, demonstrating the development of streamwise vorticity from preexisting crosswise vorticity. The black curves represent the edges of the "river"; green circles represent the location of a representative parcel at times t_0 and $t_0+\Delta t$; the red dotted arrow represents the streamline along which the parcel travels; purple line segment CD represents the vortex line in which the parcel lies; and blue line segment AB represents the parcel's instantaneous horizontal velocity vector. As the parcel enters the riverbend at time t_0, its horizontal vorticity is entirely crosswise. Because flow around the bend generates no vertical vorticity to a first approximation, AB and CD must rotate in opposite directions. Adapted from Davies-Jones et al. (2001, their Fig. 5.15).

displayed in Fig. 9. These parcels are initialized in a dense grid pattern ($dx = 25$ m) of size 1 km × 1 km centered on the vortex at 400 m AGL, and those with $\zeta \geq 0.1\,\mathrm{s}^{-1}$ at the initialization time are integrated backward in time for 900 s; this is the set of parcels plotted in Fig. 9. For our analysis, parcels that descend below 10 m AGL at any point in the integration are excluded from further analysis. We also exclude those parcels with $\zeta \geq 0.025\,\mathrm{s}^{-1}$ at any time earlier than 60 s before initialization (to exclude parcels that were circling the vortex for an extended time, rather than entering it 60 s or less prior to our initialization time).

Figure 14 presents box-and-whisker plots for the time-integrated contribution of source terms to horizontal crosswise (Figs. 14a–c) and streamwise (Figs. 14d–f) vorticity; note that these values represent the change in vorticity owing to each term during the period beginning 900 s before initialization within the vortex and ending 60 s before initialization. The 60 s before initialization is, on average, approximately the time at which stretching becomes the dominant source of cyclonic ζ generation for a parcel; we are interested in the vorticity evolution before stretching increases ζ exponentially.[8] For both horizontal crosswise and streamwise vorticity, and for all three trajectory initialization times, the signs of the median value for all five source terms agree with the terms presented for the RP; furthermore, their relative magnitudes are also qualitatively similar to those for the RP. In particular, mixing is the dominant source of positive crosswise generation, while exchange is the dominant source for positive streamwise generation. Baroclinic generation is at least an order of magnitude smaller than mixing and exchange in all cases.

Figure 15 presents analogous box-and-whisker plots for source terms of ζ. For all initialization times, tilting of streamwise vorticity has a positive contribution to cyclonic ζ for at least 75% of the parcels. Tilting of crosswise vorticity also has a positive contribution to cyclonic ζ, which tends to be smaller for most parcels, although it is quite large for a small minority of parcels. Thus, tilting of streamwise vorticity is an important source of vertical vorticity for virtually all parcels, while tilting of crosswise vorticity is also important for a smaller subset of parcels. It should be emphasized that the values in Fig. 15 represent an integrated contribution that includes a long period during which parcels are approaching the vortex from the far field. As such, a series of different physical processes occurring at different stages of a parcel's approach may be represented; for example, tilting of crosswise vorticity into cyclonic vorticity is unlikely to occur within or very near the vortex[9] but may occur earlier, during the parcel's approach. It is worth noting that among three pretornadic areas of vorticity preceding a tornado simulated in S14, one area of positive vertical vorticity (called V2 in their paper) mainly arose from the tilting of crosswise vorticity, suggesting that the role of the direct tilting of crosswise vorticity can be case dependent. In general, Figs. 14 and 15 instill confidence in the conclusions we obtain based on the analyses of the RP, and similar processes appear to persist from the PTV stage (1440 s) through the mature tornado stage (1560 s).

Figure 16 presents the total horizontal vorticity vector difference between the two experiments (FWFRIC − EnvFRIC) at 10 m AGL and 1410 s (PTV stage), with the horizontal path of the RP and the horizontal wind vectors from FWFRIC overlaid for context. It is apparent that the horizontal vorticity magnitude is substantially larger in FWFRIC than in EnvFRIC throughout most of the low-level mesocyclone, and the difference vectors are

[8] Also, once a parcel enters the vortex, the horizontal source terms often become both large in magnitude and erratic; including the integrated contributions from this period can overwhelm the signal from the preceding physical processes we aim to quantify.

[9] It should be expected that most of the parcel's horizontal vorticity is streamwise as it ascends into the tornado. In the case of substantial crosswise vorticity, a dipole of cyclonic and anticyclonic vorticity would be expected instead of the strong cyclonic vortex that occurs in FWFRIC.

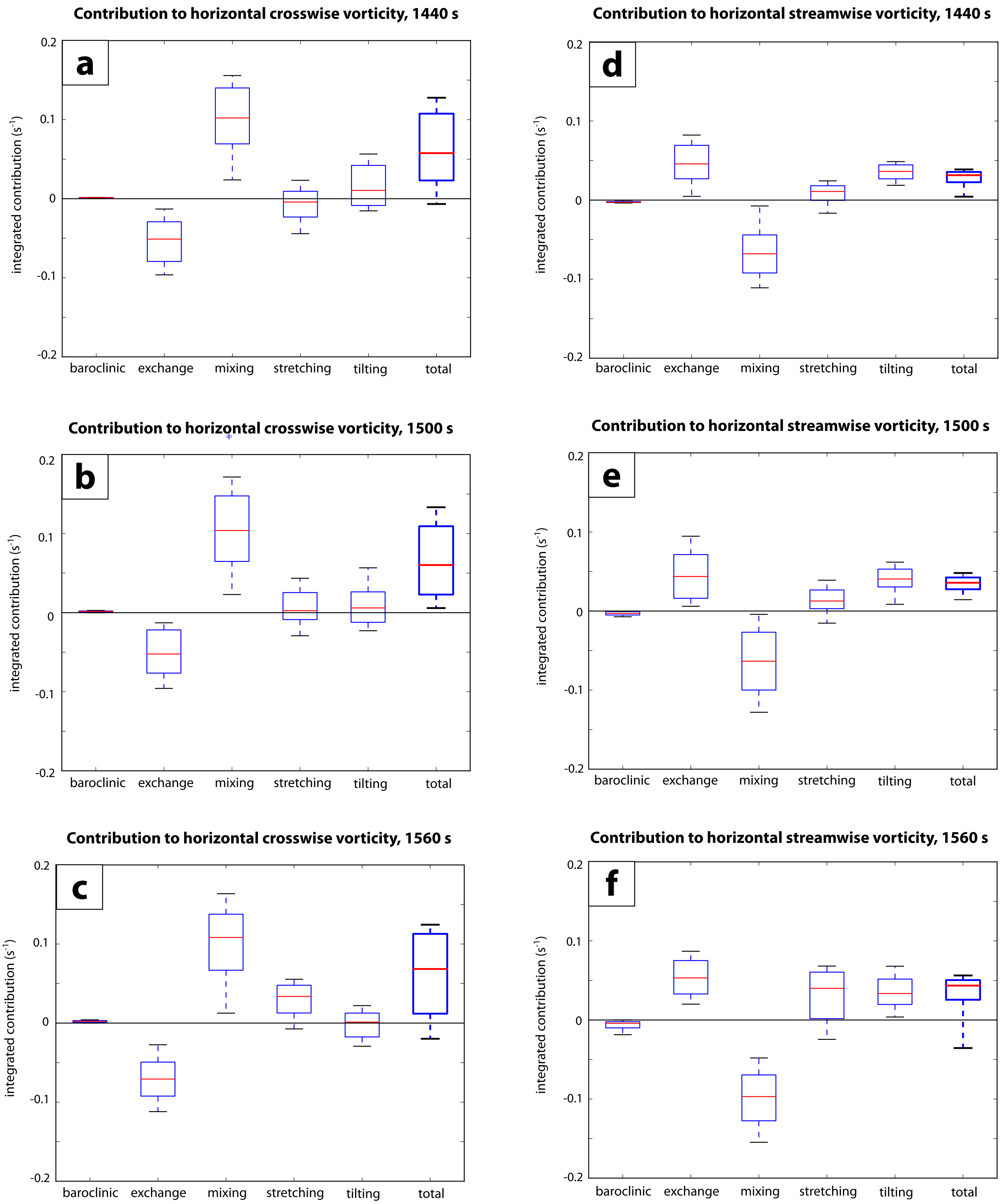

FIG. 14. Box-and-whisker plot of the time-integrated contributions of source terms to horizontal crosswise vorticity for parcels entering the (a) PTV at 1440 s, (b) tornado at 1500 s, and (c) tornado at 1560 s. (d)–(f) As in (a)–(c), but for horizontal streamwise vorticity. The terms are integrated beginning 900 s before, and ending 60 s before, the trajectories' initialization within the PTV/tornado (1440, 1500, and 1560 s, respectively). For each source term on a plot, the red line denotes the median value; the box encompasses the interquartile range; and the whiskers extend outward to the 10th (on the bottom)- and 90th (on the top)-percentile values.

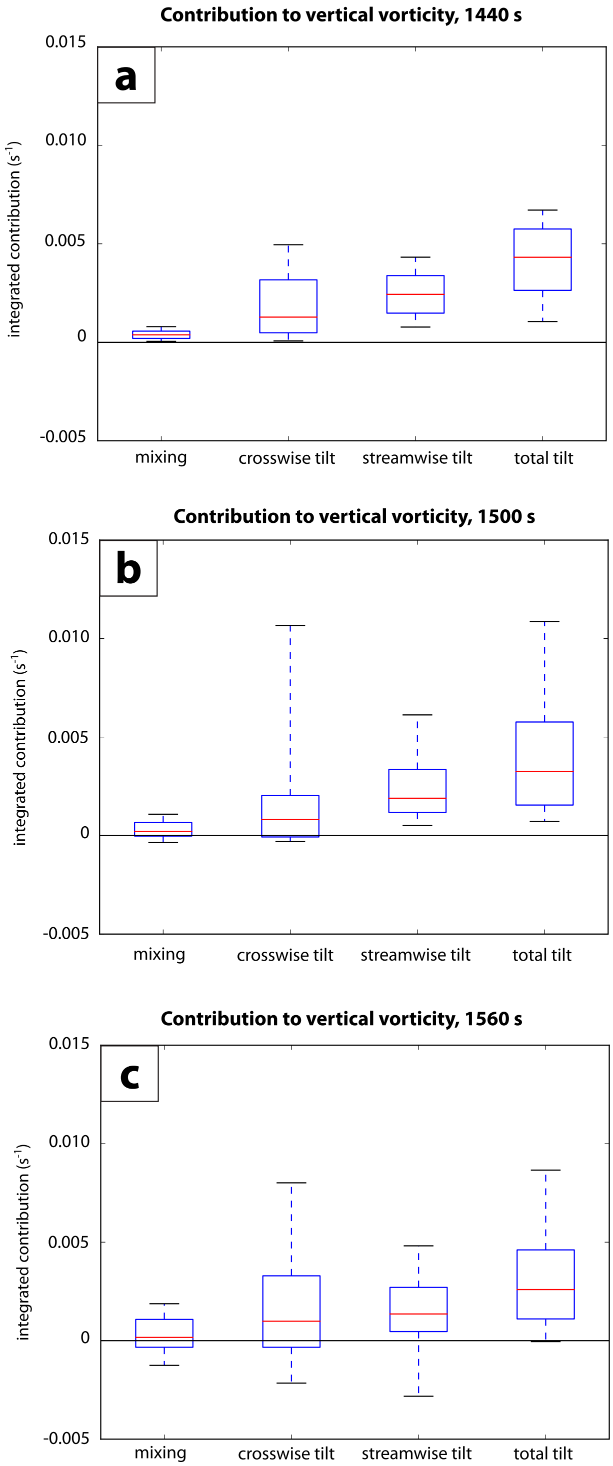

FIG. 15. Box-and-whisker plot of the time-integrated contribution to vertical vorticity for parcels entering the (a) PTV at 1440 s, (b) tornado at 1500 s, and (c) tornado at 1560 s. The plot details and time periods of integration are as described in Fig. 14.

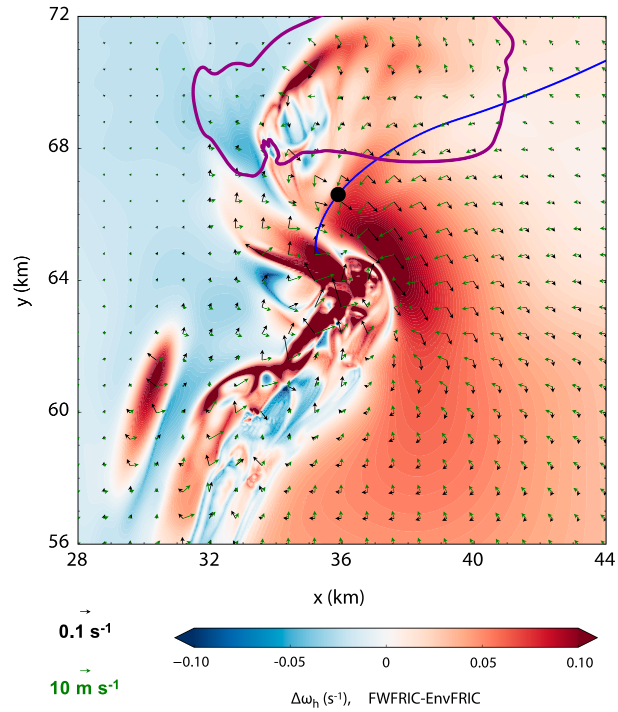

FIG. 16. Experiment difference field (FWFRIC − EnvFRIC) at 1410 s for total horizontal vorticity at 10 m AGL (black vectors), with the magnitude shaded. Horizontal ground-relative wind vectors (green) for the FWFRIC experiment (not the vector wind difference) are overlaid for context. The heavy purple contour is the 0.3 g kg^{-1} contour for rainwater mixing ratio in FWFRIC, indicating the position of the precipitation-driven downdraft; the contour for EnvFRIC (not shown) is qualitatively similar. The horizontal path of the RP (which enters the tornado in FWFRIC at 1500 s) is overlaid as a blue curve; its position at 1410 s is denoted by the black dot.

predominantly crosswise. The RP, along with a large majority of the tornado-entering trajectories in Fig. 9, passes through the northwestern extent of this frictionally enhanced vorticity region during the final several minutes of its approach to the vortex.

Figure 17 presents the vertical vorticity field at 10 m AGL at 1500 s in the region immediately surrounding the incipient tornado. At least two "feeder bands" of enhanced vertical vorticity, analogous to those presented in D14 and Nowotarski et al. (2015), can be seen extending radially outward to the north from the vortex. The leftmost band, which protrudes northwestward from the tornado, is a persistent feature feeding into the PTV at 10 m AGL for at least 180 s prior to tornadogenesis (not shown). Its location corresponds to the area through which many of our vortex-entering parcels translate along the ground during the 60–120 s immediately prior to ascending, providing evidence that even parcels that enter the vortex at lower heights than our trajectories (i.e., below 400 m AGL) are gaining cyclonic vorticity near the ground as they approach. This helps to

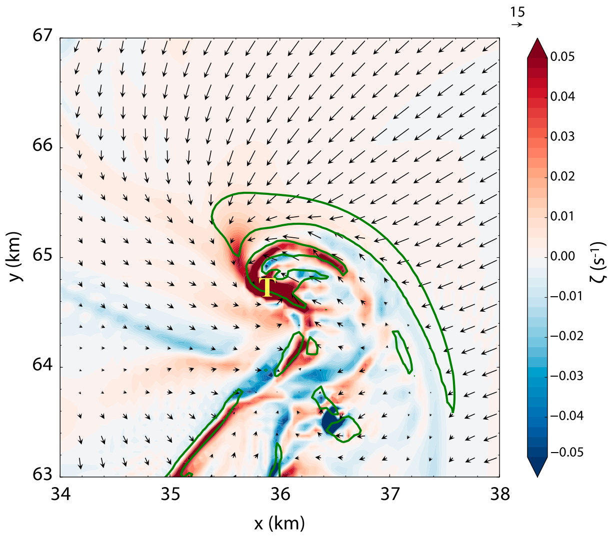

FIG. 17. Vertical vorticity (shaded), $0.05\,s^{-1}$ horizontal convergence contour (green), and storm-relative horizontal wind vectors at 10 m AGL and 1500 s in FWFRIC. Tornado location is denoted by the yellow T.

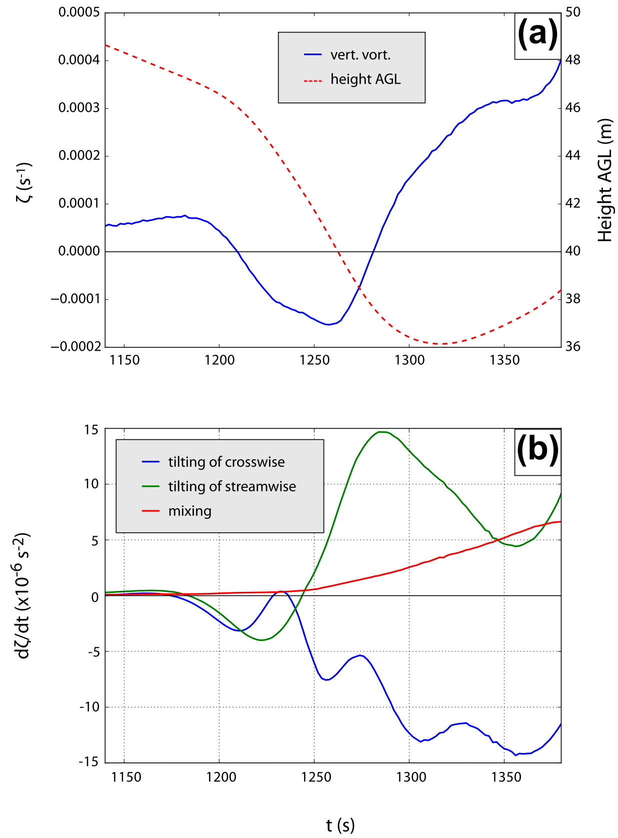

FIG. 18. Along-trajectory time series for the RP of (a) vertical vorticity (solid blue) and height AGL (dashed red) and (b) vertical vorticity generation owing to tilting of crosswise vorticity (blue), tilting of streamwise vorticity (green), and mixing (red). The time series is from 1140 to 1380 s.

bolster confidence that our vorticity budgets for vortex-entering parcels at 400–600 m AGL should qualitatively resemble those for parcels entering the vortex at heights closer to the ground. The cyclonic vorticity in the feeder bands likely originates from the tilting of horizontal vorticity primarily generated by friction as parcels approach the developing tornado, based on our earlier analysis.

c. Origin of near-ground vertical vorticity

To this point, our trajectory analysis has addressed the dominant sources for tornadic vorticity in FWFRIC; we now turn our attention to a slightly earlier time in the simulation to examine the initial development of cyclonic ζ near the ground. In the absence of preexisting vertical vorticity, horizontal vorticity generated by surface drag, baroclinity, or any other mechanism must be tilted into the vertical before it can be stretched into tornado intensity. Davies-Jones (1982, hereafter DJ82) argued that, in the absence of an extreme preexisting horizontal gradient of vertical velocity w, tilting of horizontal vorticity by an updraft alone cannot produce tornado-strength ζ near the ground, as the tilting occurs while parcels move away from the ground. This thinking has influenced subsequent studies concerning tornadogenesis dynamics and was reiterated by Davies-Jones and Markowski (2013), who demonstrated numerically and analytically the inefficiency of upward vorticity tilting near the ground even for their ''worst-case scenario'' with strong baroclinity and abruptly changing w along a gust front. In the present study, much of the cyclonic ζ generation by tilting occurs during ascent into the vortex. However, nearly all vortex-entering parcels experience a shallow descent (on the order of 10 m vertical displacement) several minutes prior to entering the vortex, which we will now analyze. Figure 18a presents a time series of ζ and height AGL for the RP between 1140 and 1380 s. The parcel descends gradually from 48 to 36 m AGL between 1140 and 1320 s. While a tendency toward anticyclonic ζ is evident initially, this trend reverses around 1260 s, after which time cyclonic ζ generation continues through the remainder of the descent. Crucially, the increase in ζ seen in Fig. 18a from 1260 s onward does not await ascent into the vortex but instead begins during this shallow descent.[10]

[10] While the parcel does not acquire large cyclonic vorticity ($\zeta > 0.01\,s^{-1}$) until its ascent is underway, cyclonic vorticity initially develops near the ground during descent, allowing for subsequent amplification by stretching.

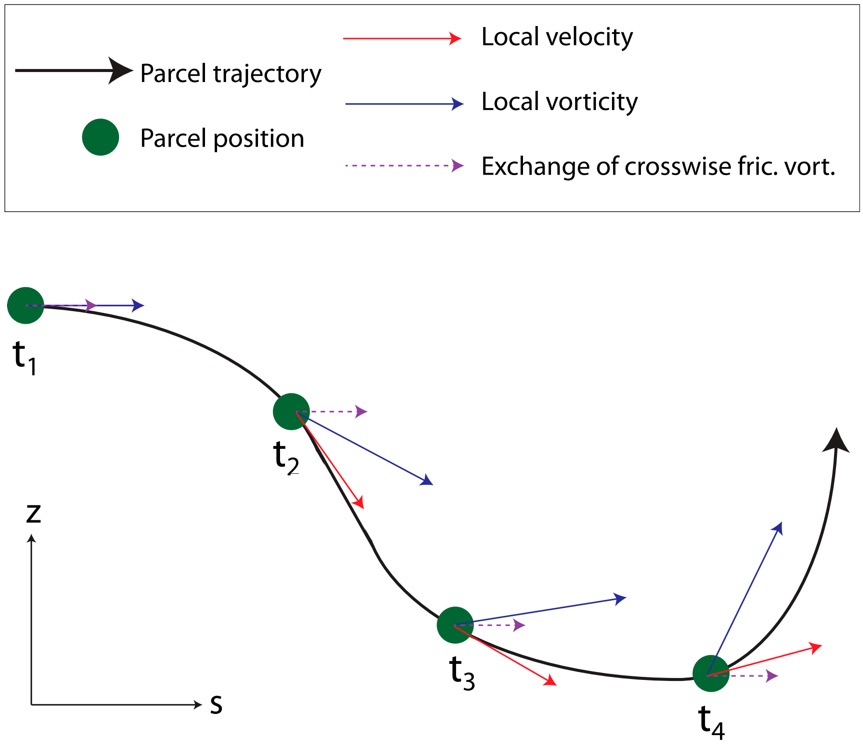

FIG. 19. Conceptual schematic depicting the evolution of parcel vorticity along a descending, vortex-entering trajectory. From times t_1 through t_4 (higher subscript indicates later in time) the parcel position (green dot), local velocity vector (solid red), local vorticity vector (solid blue), and local vorticity generation by crosswise–streamwise exchange (dashed purple) are illustrated in the s–z plane. Between t_1 and t_3, the change in the trajectory-relative vorticity vector is due to the generation of new horizontal streamwise vorticity (primarily the exchange of frictionally generated horizontal crosswise vorticity into the streamwise direction by the riverbend effect). Note that the vorticity and vorticity generation vectors represent projections into the s–z plane and neglect any crosswise component. Note also that the vorticity generation denoted by the dashed purple vectors is due to the conversion of initially crosswise vorticity (generated directly by friction) into streamwise vorticity via the riverbend effect.

A time series of ζ source terms between 1140 and 1380 s is presented in Fig. 18b. Early in the descent period, between 1180 and 1240 s, tilting of both streamwise and crosswise components results in a negative time tendency for ζ. However, the streamwise term becomes positive around 1240 s and increases in magnitude thereafter until around 1300 s. The crosswise term remains negative and also increases in magnitude, but its magnitude is smaller than the streamwise term from 1250 to 1300 s. Thus, during the RP's descent, it is primarily tilting of the streamwise component of horizontal vorticity that enables the development of cyclonic ζ, with mixing generation playing a secondary role (details of which are left for future work).

If the RP's vorticity during descent owed its existence entirely to the background environmental wind shear (which is associated with purely horizontal vorticity that is predominantly streamwise near the ground), one would not expect cyclonic ζ to develop until the parcel reached its nadir and began ascending.[11] However, in Fig. 18a, ζ first becomes cyclonic around 1280 s as descent is still ongoing. This suggests horizontal streamwise vorticity is being generated during descent. Davies-Jones and Brooks (1993, hereafter DB93) described a mechanism by which "slippage" of vortex lines with respect to the parcel trajectory allows ζ to develop during descent. In DB93, baroclinic generation of streamwise horizontal vorticity acts to "peel" a vortex line passing through the parcel upward off the local streamline during descent, which in turn allows the

[11] In the approximation of inviscid, steady flow subject only to conservative body forces, Helmholtz's first vorticity theorem states that vortex lines are material lines. As such, initially streamwise parcel vorticity cannot be tilted upward while the parcel is descending, as this would require the vortex line through the parcel to separate from its original material line.

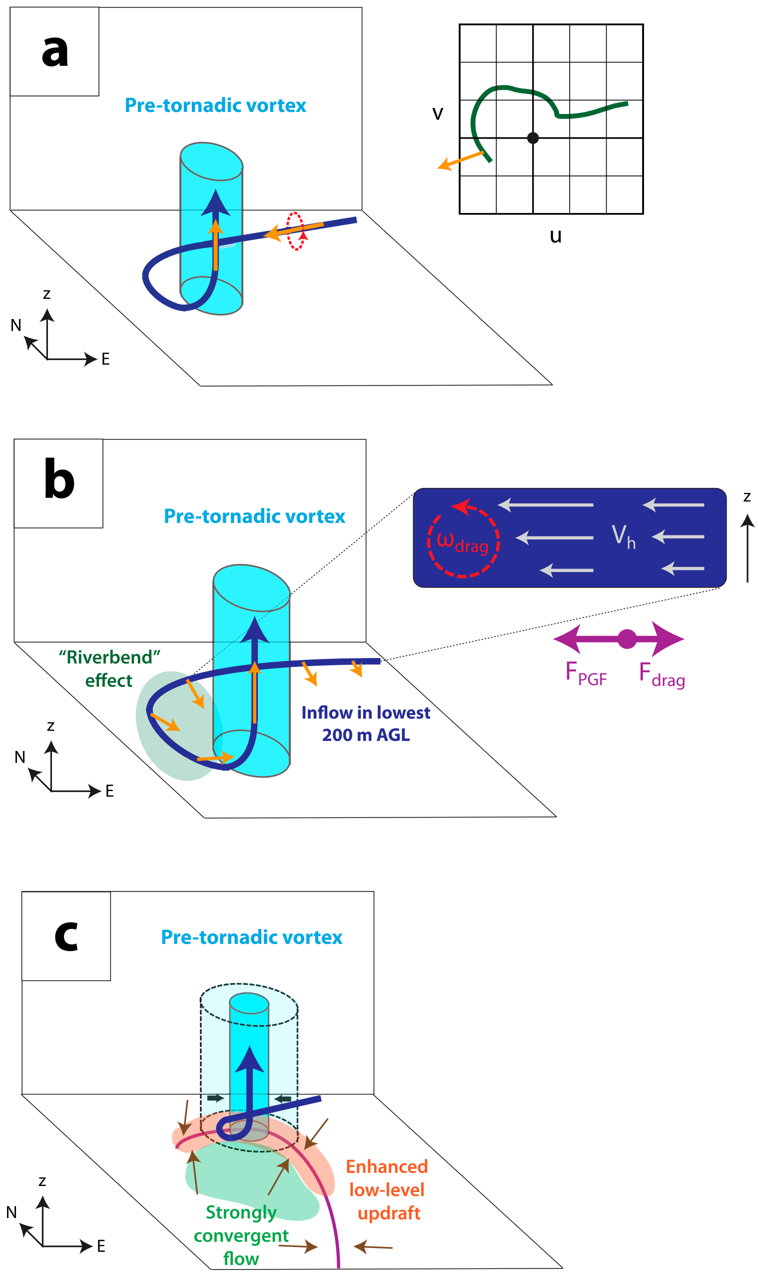

FIG. 20. Schematic illustrating physical mechanisms by which drag influences tornadogenesis in FWFRIC: (a) mechanism I, (b) mechanism II, and (c) mechanism III. For all three panels, the heavy dark blue curve with arrow is a representative storm-relative parcel trajectory entering the PTV below 500 m AGL. In (a), orange vectors are environmental vorticity vectors, with an accompanying red rotational vector denoting the sense of rotation; the subplot on the right is a representative storm-relative environmental hodograph (green) and associated near-ground vorticity vector (orange). In (b), orange vectors are the frictionally generated vorticity vectors along the trajectory; for the inset vertical cross section on the right, gray vectors represent horizontal wind, dashed red rotational arrows denote sense of vorticity, and purple arrows denote forces acting upon a parcel. In (c), the purple curve denotes the low-level convergent boundary; the larger light blue cylinder (enclosed in dashed lines) is PTV at some initial time, while the narrower medium blue cylinder (enclosed in solid lines) is PTV at some later time; inward-pointing black arrows denote contraction of the vortex with time; beige arrows denote low-level horizontal flow; orange shading denotes enhanced low-level updraft above the boundary; and green shading denotes the region of more convergent flow toward the boundary in presence of surface friction.

surrounding flow to increase the inclination angle of the vortex line via tilting. In this way, cyclonic ζ may develop during descent. More recently, S14 identified an analogous effect that relies upon initially crosswise frictionally generated vorticity that is subsequently exchanged into the streamwise direction. The authors of S14 did caution that, while evidence for a dominant frictional role was compelling for their case, the limited time window of their vorticity budgets left open the possibility of important baroclinic generation (as described by DB93) earlier in the parcel's history. In the present study, it is clear from Fig. 12c that baroclinic generation is negligible relative to other terms throughout the RP's descent. Instead, Figs. 12b and 12c suggest the S14 mechanism, whereby horizontal crosswise vorticity is generated frictionally and then exchanged into the streamwise direction as the parcel curves cyclonically. This generation of new horizontal streamwise vorticity allows the parcel's vorticity vector in the streamwise-height plane to peel upward off the trajectory during the early part of the RP's descent period and ultimately gain a cyclonic component later in the period (Fig. 19). By the time the parcel reaches its nadir, cyclonic ζ is already established. Regarding the role of baroclinic vorticity generation, the tornado forms in FWFRIC before a strong cold pool is established, increasing our confidence that it did not play a substantial role in tornadogenesis in this simulation.

Details of the formation of the weak downdraft traversed by vortex-entering parcels are left for future work. Many vortex-entering trajectories (including the RP) briefly traverse the first precipitation to reach the ground for a period of 30–60 s, coincident with their steepest period of descent; nonetheless, the RP never encounters cold outflow ($\theta' < -1$ K) during its approach to the tornado.

4. Summary and conceptual model

In two idealized supercell experiments differentiated solely by the surface drag formulation, a strong tornado develops only in the experiment where surface drag is applied to the storm-induced perturbation wind field. In the experiment with drag applied only to the background environmental wind, transient and shallow vortices develop along a convergence boundary, but no sustained tornado develops. Based on the analysis of the simulations, a conceptual model that highlights the possible roles of surface friction in tornadogenesis through three mechanisms is proposed (Fig. 20):

Mechanism I: Generation of near-surface horizontal vorticity in the environment.

The existence of surface drag creates substantial background environmental wind shear at the low levels, especially within the lowest 200 m AGL. Associated with this shear is large horizontal vorticity, which can be tilted into the vertical and stretched to produce a low-level mesocyclone. This horizontal vorticity can also contribute to the vorticity within a tornado when a low-level inflow parcel eventually enters the tornado vortex. This frictional effect acts primarily on the synoptic scale, impacting the storm environment by creating an Ekman spiral type wind profile in the boundary layer.

Mechanism II: Generation of near-surface horizontal vorticity within and around the convective storm.

Surface drag locally enhances horizontal vorticity within the lowest 100 m AGL within the convective storm and in the vicinity of the low-level mesocyclone. Here, horizontal accelerations associated with strong low-level convergence underneath the storm updraft enable surface drag to generate new horizontal crosswise vorticity. The vortex-entering parcels typically have cyclonically curved paths during their approach to the mesocyclone, and crosswise vorticity is continuously exchanged into the streamwise direction via the riverbend effect; this vorticity can subsequently be tilted into the vertical and be stretched. For descending parcels, such tilting into the vertical can occur even before they reach their minimum height, creating cyclonic vorticity before the trajectory turns abruptly upward (very near the ground, in some cases). The tilting of frictionally generated horizontal vorticity into the vertical can also contribute to the enhancement of the low-level mesocyclone in the pretornadic phase; the mesocyclone and associated low-level updraft in turn modulate the above processes.

Mechanism III. Enhancement of low-level convergence beneath the mesocyclone.

During the development of the low-level mesocyclone, a stronger and more concentrated region of low-level convergence is found in the presence of surface drag. This strengthens the low-level updraft, setting up a favorable configuration for stretching to amplify cyclonic vorticity to tornado strength. This mechanism also acts on the storm scale.

Mechanism I is inherent in the friction-balanced sounding used to initialize both EnvFRIC and FWFRIC and thus operates in both. By contrast, mechanisms II and III each require surface drag to operate on storm-generated perturbation wind components and thus are present only in FWFRIC. Because a strong tornado develops in FWFRIC while only a brief, subtornadic vortex develops in EnvFRIC, we conclude that some combination of mechanisms II and III is responsible for instigating tornadogenesis in this case. In fact, both processes may be necessary for the tornado to form in FWFRIC. One fortuitous property of these results is that the tornado develops quite early relative to the parent supercell's life cycle. At this early stage, discrepancies between the model fields in FWFRIC and EnvFRIC are still minor away from the low-level mesocyclone; nonlinear effects have not yet amplified these discrepancies into important differences at the storm scale. As a result, comparison between the results of the two experiments is relatively straightforward and can confidently be attributed to the difference in friction.

Of notable absence is baroclinic vorticity generation as an important mechanism for vortex genesis in our case. In fact, backward trajectories for parcels entering the tornado incur negligible baroclinic generation of horizontal vorticity during their approach. This result should be interpreted as evidence that a combination of environmental and locally generated frictional horizontal vorticity potentially can be sufficient for tornadogenesis under certain circumstances. This does not, however, preclude the likely existence of other modes for supercell tornadogenesis; indeed, it should be expected that the mechanisms for tornadoes forming within more mature storms featuring well-developed RFDs will differ at least in some details, including the role of baroclincally generated vorticity. Even so, this study corroborates the mechanism identified in S14 in which horizontal vorticity generated by surface drag can be a significant or even dominant contributor to tornadic vorticity. Note that, even in our case, where baroclinic vorticity is shown to play a negligible role in tornadogenesis, a downdraft (albeit shallow) is still necessary for developing meaningful cyclonic vorticity very close to the ground. It is also worth noting that Markowski et al. (2015) recently presented preliminary results from highly idealized "toy model" pseudostorm simulations that included drag. One of their simulations produced an early tornado away from the cold pool with striking similarities to the tornado in FWFRIC herein; tilting of frictionally enhanced horizontal vorticity by a downdraft near the ground (speculated to represent "compensating subsidence" on the periphery of the updraft) was implicated in vortex genesis.

In FWFRIC, the tornado formed very quickly and at a large distance from any precipitation or baroclinic gradients; while such occurrences may be atypical among observed supercell tornadoes, they are not without precedent. For example, Palmer et al. (2011) documented a strong tornado (denoted B2 in their Fig. 7a) during the 10 May 2010 Oklahoma outbreak located several kilometers east-southeast of the parent storm's 35-dBZ reflectivity contour, which occurred within 30 min of the storm's first radar echoes. For some cases with a similar apparent lack of baroclinic vorticity, preexisting cyclonic ζ in the local environment (e.g., associated with a surface boundary or low pressure center) could plausibly be an important source of tornadic vorticity. In our idealized simulations, however, no such direct sources of vertical vorticity exist in the prestorm environment. Perhaps, given sufficiently strong low-level shear and/or surface roughness, tornadoes qualitatively similar to the tornado in FWFRIC can develop in the real world, even if they do not represent the most common mode of supercell tornadogenesis.

To highlight potential influences of drag upon tornadogenesis, we deliberately chose a drag coefficient $C_d = 0.01$, which is a relatively large value over land. Furthermore, in our simulation, the subgrid-scale turbulence mixing is parameterized by a 1.5-order TKE closure scheme at a large-eddy simulation (LES) resolution. As described by Mason and Thomson (1992) and Brasseur and Wei (2010), LES turbulence schemes tend to overestimate the velocity gradient near a rigid wall (in this case, the vertical gradient of horizontal velocity at the lowest few grid levels above ground). With these considerations in mind, it is probable that our simulations exaggerate the effect of drag to some extent, relative to a typical supercell case over land. The quantitative treatment of surface drag and near-surface turbulence mixing will require further research. Still, qualitatively, we believe the effects of surface drag on tornadogenesis investigated herein should be valid.

This study uses two idealized experiments to illustrate mechanisms by which surface drag can instigate tornadogenesis, so additional work is needed to clarify these mechanisms' relative importance and under which conditions they operate most effectively. When a classical precipitation-loaded RFD is present and tornado-entering parcels traverse regions of significant baroclinity, will storm-scale frictional generation still be a dominant source of tornadic vorticity? Is there a threshold on the drag coefficient required for mechanisms II and III to enter a positive feedback cycle that produces a sustained tornado? How, if at all, do the qualitative results presented herein change when a much finer vertical grid spacing is used near the ground? What were the primary forces driving the descent and ascent of the vortex-entering parcels? These are some of the questions that will be addressed in future work.

Acknowledgments. Detailed comments and suggestions of three anonymous reviewers significantly improved the original manuscript. This work was primarily supported by NSF Grant AGS-0802888. The second author was also supported by NSF Grants AGS-1046171 and AGS-1261776. Numerical simulations were performed at the Texas Advanced Supercomputing Center, an NSF XSEDE facility.

REFERENCES

Adlerman, E. J., and K. K. Droegemeier, 2002: The sensitivity of numerically simulated cyclic mesocyclogenesis to variations in model physical and computational parameters. *Mon. Wea. Rev.*, **130**, 2671–2691, doi:10.1175/1520-0493(2002)130<2671:TSONSC>2.0.CO;2.

Brasseur, J. G., and T. Wei, 2010: Designing large-eddy simulation of the turbulent boundary layer to capture law-of-the-wall scaling. *Phys. Fluids*, **22**, 021303, doi:10.1063/1.3319073.

Dahl, J. M. L., 2015: Near-ground rotation in simulated supercells: On the robustness of the baroclinic mechanism. *Mon. Wea. Rev.*, **143**, 4929–4942, doi:10.1175/MWR-D-15-0115.1.

——, M. D. Parker, and L. J. Wicker, 2012: Uncertainties in trajectory calculations within near-surface mesocyclones of simulated supercells. *Mon. Wea. Rev.*, **140**, 2959–2966, doi:10.1175/MWR-D-12-00131.1.

——, ——, and ——, 2014: Imported and storm-generated near-ground vertical vorticity in a simulated supercell. *J. Atmos. Sci.*, **71**, 3027–3051, doi:10.1175/JAS-D-13-0123.1.

Davies-Jones, R., 1982: Observational and theoretical aspects of tornadogenesis. *Intense Atmospheric Vortices*, L. Bengtsson and J. Lighthill, Eds., Topics in Atmospheric and Oceanographic Sciences, Springer-Verlag, 175–189.

——, 1984: Streamwise vorticity: The origin of updraft rotation in supercell storms. *J. Atmos. Sci.*, **41**, 2991–3006, doi:10.1175/1520-0469(1984)041<2991:SVTOOU>2.0.CO;2.

——, 2015: A review of supercell and tornado dynamics. *Atmos. Res.*, **158–159**, 274–291, doi:10.1016/j.atmosres.2014.04.007.

——, and H. Brooks, 1993: Mesocyclogenesis from a theoretical perspective. *The Tornado: Its Structure, Dynamics, Prediction, and Hazards*, C. Church et al., Eds., Amer. Geophys. Union, 105–114.

——, and P. Markowski, 2013: Lifting of ambient air by density currents in sheared environments. *J. Atmos. Sci.*, **70**, 1204–1215, doi:10.1175/JAS-D-12-0149.1.

——, R. J. Trapp, and H. B. Bluestein, 2001: Tornadoes and tornadic storms. Severe Convective Storms, *Meteor. Monogr.*, No. 50, Amer. Meteor. Soc., 167–221, doi:10.1175/0065-9401-28.50.167.

Dawson, D. T., M. Xue, J. A. Milbrandt, and M. K. Yau, 2010: Comparison of evaporation and cold pool development between single-moment and multimoment bulk microphysics schemes in idealized simulations of tornadic thunderstorms. *Mon. Wea. Rev.*, **138**, 1152–1171, doi:10.1175/2009MWR2956.1.

——, ——, ——, and A. Shapiro, 2015: Sensitivity of real-data simulations of the 3 May 1999 Oklahoma City tornadic supercell and associated tornadoes to multimoment microphysics. Part I: Storm- and tornado-scale numerical forecasts. *Mon. Wea. Rev.*, **143**, 2241–2265, doi:10.1175/MWR-D-14-00279.1.

Grzych, M. L., B. D. Lee, and C. A. Finley, 2007: Thermodynamic analysis of supercell rear-flank downdrafts from project ANSWERS. *Mon. Wea. Rev.*, **135**, 240–246, doi:10.1175/MWR3288.1.

Klemp, J. B., and R. Rotunno, 1983: A study of the tornadic region within a supercell thunderstorm. *J. Atmos. Sci.*, **40**, 359–377, doi:10.1175/1520-0469(1983)040<0359:ASOTTR>2.0.CO;2.

Lemon, L. R., and C. A. Doswell, 1979: Severe thunderstorm evolution and mesocyclone structure as related to tornadogenesis. *Mon. Wea. Rev.*, **107**, 1184–1197, doi:10.1175/1520-0493(1979)107<1184:STEAMS>2.0.CO;2.

Lewellen, W. S., D. C. Lewellen, and R. I. Sykes, 1997: Large-eddy simulation of a tornado's interaction with the surface. *J. Atmos. Sci.*, **54**, 581–605, doi:10.1175/1520-0469(1997)054<0581:LESOAT>2.0.CO;2.

Lin, Y.-L., R. D. Farley, and H. D. Orville, 1983: Bulk parameterization of the snow field in a cloud model. *J. Climate Appl. Meteor.*, **22**, 1065–1092, doi:10.1175/1520-0450(1983)022<1065:BPOTSF>2.0.CO;2.

Markowski, P., and Y. P. Richardson, 2014: The influence of environmental low-level shear and cold pools on tornadogenesis: Insights from idealized simulations. *J. Atmos. Sci.*, **71**, 243–275, doi:10.1175/JAS-D-13-0159.1.

——, J. M. Straka, and E. N. Rasmussen, 2002: Direct surface thermodynamic observations within the rear-flank downdrafts of nontornadic and tornadic supercells. *Mon. Wea. Rev.*, **130**, 1692–1721, doi:10.1175/1520-0493(2002)130<1692:DSTOWT>2.0.CO;2.

——, Y. Richardson, E. Rasmussen, J. Straka, R. Davies-Jones, and R. J. Trapp, 2008: Vortex lines within low-level mesocyclones obtained from pseudo-dual-doppler radar observations. *Mon. Wea. Rev.*, **136**, 3513–3535, doi:10.1175/2008MWR2315.1.

——, and Coauthors, 2012: The pretornadic phase of the Goshen County, Wyoming, supercell of 5 June 2009 intercepted by VORTEX2. Part II: Intensification of low-level rotation. *Mon. Wea. Rev.*, **140**, 2916–2938, doi:10.1175/MWR-D-11-00337.1.

——, Y. Richardson, and G. H. Bryan, 2015: How does surface drag affect the development of near-surface vertical vorticity in supercell thunderstorms? *Proc. Eighth European Conf. on Severe Storms*, Wiener Neustadt, Austria, European Severe Storms Laboratory, CSS2015-95. [Available online at http://meetingorganizer.copernicus.org/ECSS2015/ECSS2015-95.pdf.]

Mashiko, W., H. Niino, and T. Kato, 2009: Numerical simulation of tornadogenesis in an outer-rainband minisupercell of Typhoon Shanshan on 17 September 2006. *Mon. Wea. Rev.*, **137**, 4238–4260, doi:10.1175/2009MWR2959.1.

Mason, P. J., and D. J. Thomson, 1992: Stochastic backscatter in large-eddy simulations of boundary layers. *J. Fluid Mech.*, **242**, 51–78, doi:10.1017/S0022112092002271.

Moeng, C.-H., and J. C. Wyngaard, 1988: Spectral analysis of large-eddy simulations of the convective boundary layer. *J. Atmos. Sci.*, **45**, 3573–3587, doi:10.1175/1520-0469(1988)045<3573:SAOLES>2.0.CO;2.

Nowotarski, C. J., P. M. Markowski, Y. P. Richardson, and G. H. Bryan, 2015: Supercell low-level mesocyclones in simulations with a sheared convective boundary layer. *Mon. Wea. Rev.*, **143**, 272–297, doi:10.1175/MWR-D-14-00151.1.

Palmer, R. D., and Coauthors, 2011: Observations of the 10 May 2010 tornado outbreak using OU-PRIME: Potential for new science with high-resolution polarimetric radar. *Bull. Amer. Meteor. Soc.*, **92**, 871–891, doi:10.1175/2011BAMS3125.1.

Rotunno, R., and J. Klemp, 1985: On the rotation and propagation of simulated supercell thunderstorms. *J. Atmos. Sci.*, **42**, 271–292, doi:10.1175/1520-0469(1985)042<0271:OTRAPO>2.0.CO;2.

Schenkman, A. D., M. Xue, and A. Shapiro, 2012: Tornadogenesis in a simulated mesovortex within a mesoscale convective system. *J. Atmos. Sci.*, **69**, 3372–3390, doi:10.1175/JAS-D-12-038.1.

——, ——, and M. Hu, 2014: Tornadogenesis in a high-resolution simulation of the 8 May 2003 Oklahoma City supercell. *J. Atmos. Sci.*, **71**, 130–154, doi:10.1175/JAS-D-13-073.1.

Shabbott, C. J., and P. M. Markowski, 2006: Surface in situ observations within the outflow of forward-flank downdrafts of supercell thunderstorms. *Mon. Wea. Rev.*, **134**, 1422–1441, doi:10.1175/MWR3131.1.

Skamarock, W. C., M. L. Weisman, and J. B. Klemp, 1994: Three-dimensional evolution of simulated long-lived squall lines. *J. Atmos. Sci.*, **51**, 2563–2584, doi:10.1175/1520-0469(1994)051<2563:TDEOSL>2.0.CO;2.

Snook, N., and M. Xue, 2008: Effects of microphysical drop size distribution on tornadogenesis in supercell thunderstorms. *Geophys. Res. Lett.*, **35**, L24803, doi:10.1029/2008GL035866.

Trapp, R. J., 2000: A clarification of vortex breakdown and tornadogenesis. *Mon. Wea. Rev.*, **128**, 888–895, doi:10.1175/1520-0493(2000)128<0888:ACOVBA>2.0.CO;2.

——, and B. H. Fiedler, 1995: Tornado-like vortexgenesis in a simplified numerical model. *J. Atmos. Sci.*, **52**, 3757–3778, doi:10.1175/1520-0469(1995)052<3757:TLVIAS>2.0.CO;2.

Wicker, L. J., and R. B. Wilhelmson, 1993: Numerical simulation of tornadogenesis within a supercell thunderstorm. *The Tornado: Its Structure, Dynamics, Prediction, and Hazards*, C. Church et al., Eds., Amer. Geophys. Union, 75–88.

Xue, M., K. K. Droegemeier, and V. Wong, 2000: The Advanced Regional Prediction System (ARPS)—A multi-scale nonhydrostatic atmospheric simulation and prediction model. Part I: Model dynamics and verification. *Meteor. Atmos. Phys.*, **75**, 161–193, doi:10.1007/s007030070003.

——, and Coauthors, 2001: The Advanced Regional Prediction System (ARPS)—A multi-scale nonhydrostatic atmospheric simulation and prediction tool. Part II: Model physics and applications. *Meteor. Atmos. Phys.*, **76**, 143–165, doi:10.1007/s007030170027.

——, M. Hu, and A. D. Schenkman, 2014: Numerical prediction of the 8 May 2003 Oklahoma City tornadic supercell and embedded tornado using ARPS with the assimilation of WSR-88D data. *Wea. Forecasting*, **29**, 39–62, doi:10.1175/WAF-D-13-00029.1.